ELSEVIER

Chemical Geology 225 (2006) 40–60

CHEMICAL GEOLOGY
INCLUDING
ISOTOPE GEOSCIENCE

www.elsevier.com/locate/chemgeo

Fluorite solubility in hydrous haplogranitic melts at 100 MPa

David Dolejš *, Don R. Baker

Department of Earth and Planetary Sciences, McGill University, 3450 rue University, Montréal, QC, Canada H3A 2A7

Received 15 July 2004; received in revised form 25 July 2005; accepted 18 August 2005

Abstract

Fluorite is the most common fluoride mineral in magmatic silicic systems and its crystallization can moderate or buffer fluorine concentrations in these settings. We have experimentally determined fluorite solubility and speciation mechanisms in haplogranitic melts at 800–950 °C, 100 MPa and aqueous-fluid saturation. The starting haplogranite compositions: peraluminous (alumina saturation index, ASI = 1.2), subaluminous (ASI = 1.0) and peralkaline (ASI = 0.8) were variably doped with CaO or F_2O_{-1} in the form of stoichiometric mineral or glass mixtures. The solubility of fluorite along the fluorite–hydrous haplogranite binaries is low: 1.054 ± 0.085 wt.% CaF_2 (peralkaline), 0.822 ± 0.076 wt.% (subaluminous) and 1.92 ± 0.15 wt.% (peraluminous) at 800 °C, 100 MPa and 10 wt.% H_2O, and exhibits a minimum at ASI ~ 1. Fluorite saturation isotherms are strongly hyperbolic in the CaO–F_2O_{-1} space, suggesting that fluorite saturation is controlled by the activity product of CaO and F_2O_{-1}, i.e., these components are partially decoupled in the melt structure. The form of fluorite liquidus isotherms implies distinct roles of fluorite crystallization: in Ca-dominant systems, fluorite crystallization is controlled by the fluorine concentration in the melt only and remains nearly independent of calcium contents; in F-rich systems, the crystallization of fluorite is determined by CaO contents and it does not buffer fluorine concentration in the melt. The apparent equilibrium constant, K, for the equilibrium $CaO + cF_2O_{-1} = CaF_2$ (+associates) is $\log K = -(2.449 \pm 0.085) \cdot Al_2O_3^{exc} + (4.902 \pm 0.066)$; the reaction-stoichiometry parameter varies as follows: $c = -(0.92 \pm 0.11) \cdot Al_2O_3^{exc} + (1.042 \pm 0.084)$ at 800 °C, 100 MPa and fluid saturation where $Al_2O_3^{exc}$ are molar percent alumina in excess over alkali oxides. The reaction stoichiometry, c, changes at subaluminous composition: in peralkaline melts, competition of other network modifiers for excess fluorine anions leads to the preferential alkali–F short-range order, whereas in peraluminous compositions, excess alumina associates with calcium cations to form calcioaluminate tetrahedra. The temperature dependence of fluorite solubility is described by the binary symmetric Margules parameter, $W = 36.0 \pm 1.4$ kJ (peralkaline), 39.7 ± 0.5 kJ (subaluminous) and 32.8 ± 0.7 kJ (peraluminous). The strong positive deviations from ideal mixing imply the occurrence of CaF_2–granite liquid–liquid immiscibility at temperatures above 1258 °C, which is consistent with previous experimental data. These experimental results suggest very low solubilities of fluorite in Ca-rich melts, consistent with the lack of fluorine enrichment in peralkaline rhyolites and calc-alkaline batholiths. On the other hand, high CaO concentrations necessary to crystallize fluorite in F-rich peraluminous melts are not observed in nature and thus magmatic crystallization of fluorite in topaz-bearing silicic suites is suppressed. A procedure for calculating fluorite solubility and the liquidus isotherms for a whole-rock composition and temperature of interest is provided.

Keywords: Fluorite; Crystallization; Granite; Rhyolite; Melt; Thermodynamics

1. Introduction

Fluorite, CaF_2, is the most common fluoride mineral in silicic magmatic rocks and their metamorphic and

* Corresponding author. Present address: Bayerisches Geoinstitut, University of Bayreuth, D-95440 Bayreuth, Germany. Tel.: +49 921 553717; fax: +49 921 553769.
E-mail address: david.dolejs@uni-bayreuth.de (D. Dolejš).

0009-2541/$ - see front matter © 2005 Elsevier B.V. All rights reserved.
doi:10.1016/j.chemgeo.2005.08.007

metasomatic successors (Burt, 1972; Bohlen and Essene, 1978; Hogan and Gilbert, 1995; Haapala, 1997; Marshall et al., 1998; Sallet et al., 2000). Its abundance varies from accessory to percent amounts in granites and rhyolites (Buddington and Leonard, 1962; Hogan and Gilbert, 1995; Marshall et al., 1998; Sallet et al., 2000; Abdel-Rahman and El-Kibbi, 2001), and it is irregularly distributed in pegmatites and greisens (Simmons and Heinrich, 1975; Lentz and Gregoire, 1995; Haapala, 1997; Sakoma et al., 2000; Frindt and Poutiainen, 2002).

Despite of the widespread occurrence of fluorite in magmatic and hydrothermal rock types, there appears to be no obvious relationship between bulk-rock calcium or fluorine contents. Natural observations, however, point to effects of magma aluminosity on fluorite crystallization. Fluorite occurs as volcanic phenocrysts, solid inclusions in magmatic phenocrysts and microlites in melt inclusions in peralkaline suites (e.g., Marshall et al., 1998; Webster and Rebbert, 2001). It becomes a rare accessory phase in metaluminous granitic rocks and their metamorphic equivalents (Buddington and Leonard, 1962; Bohlen and Essene, 1978; Hogan and Gilbert, 1995; Price et al., 1999). In peraluminous systems represented by topaz-bearing granites, rhyolites and ongonites, fluorite is commonly an abundant but secondary phase formed during subsolidus alteration (Taylor et al., 1984; Lentz and Gregoire, 1995; Sakoma et al., 2000; Frindt and Poutiainen, 2002); its formation is related to decalcification of plagioclase during open-system fluorination or to hydration and temperature decrease (Barton, 1982; Ryabchikov et al., 1996; Haapala, 1997; Dolejš and Baker, 2004a).

Experimental studies reveal a similar dependence of fluorite crystallization on the system aluminosity. Phase equilibria experiments with natural peralkaline rhyolites identify fluorite as an early magmatic phase (Scaillet and Macdonald, 2001, 2004). In the metaluminous Spor Mountain vitrophyre, the fluorite liquidus is located about 150–200 °C above solidus at 50–200 MPa, indicating its late magmatic origin (Webster et al., 1987). In peraluminous topaz granites, fluorite is stable near the solidus only and melts completely within 25–40 °C, at 100–1000 MPa (Weidner and Martin, 1987; Xiong et al., 2002). These results suggest that fluorite moderates fluorine concentrations in Ca-rich peralkaline suites whereas its late appearance (or instability) with increasing peraluminosity may promote fluorine enrichment, leading to topaz granites and rhyolites (cf. Scaillet and Macdonald, 2004). It has been proposed that fluorite exhibits a minimum solubility at subaluminous composition (Scaillet and Macdonald, 2004), but crucial relationships between behavior of fluorite constituents (CaO, F), alkali oxides and alumina remain unknown.

The natural observations are further rationalized by the CaO vs. F_2O_{-1} diagram as a function of melt aluminosity (Fig. 1). This plot reveals a dichotomy between calcium and fluorine concentrations as well as the systematic distribution of peralkaline, metaluminous and peraluminous melt types. Peralkaline and metaluminous compositions are characterized by moderate to high calcium contents (up to 3.6 wt.% CaO), but very low fluorine concentrations (frequently less than 0.2 wt.% F). On the contrary, peraluminous suites are calcium-poor, with an inverse correlation between calcium content and melt peraluminosity (~0.2 and ~1.0 wt.% CaO), but produce F-rich residual melts (up to 7 wt.% F). The whole data set is limited by a hyperbolic trend that can be described by the (solubility) product of CaO and F_2O_{-1}. This finding suggests at least partially independent speciation of calcium and fluorine in the melt structure and questions the Ca–F species as the dominant melt complex (Weidner and Martin, 1987; Haapala, 1997; Tindle et al., 2002). Thus, we propose to investigate the fluorite solution mechanisms in a multicomponent space, with CaO, F_2O_{-1} and alumina saturation index (ASI; Shand, 1927; Holtz et al., 1992) as independent variables.

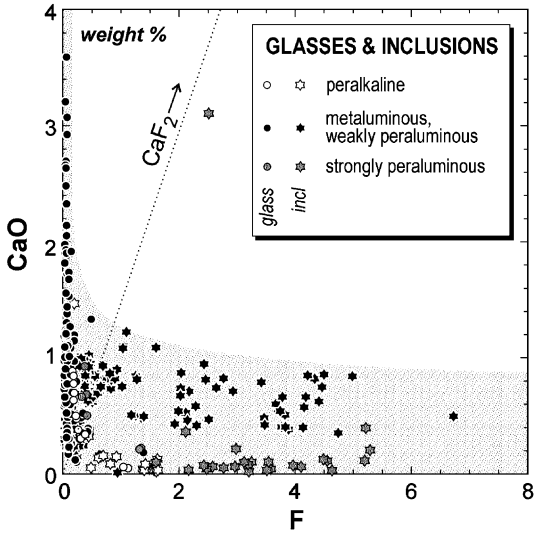

Fig. 1. CaO vs. F distribution in natural glasses and melt inclusions illustrating the dichotomy between Ca-rich metaluminous and peralkaline vs. F-rich strongly peraluminous suites. Data sources: Bailey and Macdonald (1970), Lowenstern (1994), Lowenstern et al. (1994), Macdonald et al. (1992), Mahood and Stimac (1990), Pichavant et al. (1987, 1988), Scaillet and Macdonald (2001), Thomas and Webster (2000), Webster and Duffield (1991, 1994), Webster and Rebbert (2001) and Webster et al. (1993, 1996, 1997).

Contrary to several studies in natural multicomponent systems (Price et al., 1999; Scaillet and Macdonald, 2001, 2004), previous experimental attempts to systematically determine fluorite solubility in metaluminous and peraluminous granitic melts were only partially successful (Gabitov et al., 2001; Dolejš and Baker, 2001; R. Linnen, personal communication, 2001). Interaction between fluorite and granitic melt leads to stable or metastable formation of pseudobinary calcium metasilicate (wollastonite) by the reactions:

$$(Na,K)AlSi_3O_8(l) + 2CaF_2(s) = 2CaSiO_3(s) + (Na,K)AlF_4(l) + SiO_2(l) \quad (1)$$

and/or

$$3(Na,K)AlSi_3O_8(l) + 3CaF_2(s) = 2CaSiO_3(s) + (Na,K)_3AlF_6(l) + CaAl_2Si_2O_8(l) + 5SiO_2(l) \quad (2)$$

suggesting the formation of alkali–aluminofluoride complexes in the melt structure (Schaller et al., 1992; Zeng and Stebbins, 2000; Mysen et al., 2004). In order to suppress wollastonite formation and to approach higher fluorine concentrations, as observed in natural melts, synthetic granitic compositions were gradually doped with fluorine, thus decreasing the wollastonite stability (Dolejš and Baker, 2001):

$$CaSiO_3(s) + F_2O_{-1} = CaF_2(s) + SiO_2(l). \quad (3)$$

This experimental approach reveals independent effects of CaO and F_2O_{-1} activities on fluorite solubility in silicate melts, thus may suggest partial decoupling of calcium and fluorine components in the melt (Dolejš and Baker, 2003). Subsequent extension by using various types of calcium additives (wollastonite, anorthite) confirmed this solution mechanism and allowed us to explore additional effects of melt aluminosity on fluorite solubility.

In this study we report experimental results on fluorite solubility in hydrous haplogranitic melts at 100 MPa. Three sets of synthetic granitic compositions variably doped with F_2O_{-1} or CaO provide 34 starting compositions in the K_2O–Na_2O–CaO–Al_2O_3–SiO_2–F_2O_{-1} space at 10 wt.% H_2O and cover peralkaline to peraluminous conditions with the molar ratio $Al_2O_3/(Na_2O+K_2O)=0.8$ to 1.2. These results illustrate the individual effects of CaO and F on fluorite solubility and its changes in dependence on the melt aluminosity. These provide further insights into the structural mechanisms of fluorite solubility and the possibility of the occurrence of fluoride–silicate liquid–liquid immiscibility. Finally, we relate activities (chemical potentials) of CaO and F_2O_{-1} to multiphase cotectic or solidus assemblages in order to predict relative levels of fluorine enrichment in natural multicomponent systems.

2. Experimental and analytical methodology

Base glasses (HPG-2, ALK-12, AKG-8, anorthite, wollastonite) were synthesized from K_2CO_3, Na_2CO_3, $CaCO_3$, Al_2O_3 and SiO_2, permanently stored at 120 °C. Chemical compounds were carefully weighed into an

Table 1
Chemical composition of starting materials

Symbol	*n*	SiO_2 (wt.%)	Al_2O_3	CaO	Na_2O	K_2O	F	Total	A/NK	A/CNK	Notes
HPG-2		79.47	11.73		3.90	4.91			1.00	1.00	
	16	78.37 (48)	11.53 (34)	0.0041 (53)	3.74 (13)	4.979 (94)		98.63 (24)	0.999 (36)	0.998 (36)	Glass
ALG-12		77.64	13.75		3.81	4.79			1.20	1.20	
	8	76.4 (1.1)	14.4 (1.1)	0.014 (18)	4.09 (30)	4.84 (13)		99.83 (64)	1.20 (11)	1.20 (11)	Glass
AKG-8		78.07	11.52		5.58	4.82			0.80	0.80	
	10	77.7 (1.1)	11.58 (66)	0.0065 (64)	5.71 (29)	4.70 (15)		99.72 (48)	0.800 (53)	0.799 (53)	Glass
Anorthite		43.19	36.65	20.16						1.0000	
	15	43.00 (52)	36.17 (30)	19.971 (50)	0.164 (30)	0.025 (16)		99.33 (91)		0.9880 (87)	Glass
Cryolite			24.28		44.28		54.30		0.3333	0.3333	
	10	0.011 (21)	25.65 (53)	0.012 (14)	45.67 (12)	0.010 (18)	57.29 (89)	104.51 (19)	0.3414 (71)	0.3413 (71)	Crystal
Topaz		32.65	55.40				20.64				
	18	32.62 (39)	54.64 (28)	0.008 (10)	0.049 (79)	0.0071 (84)	20.92 (13)	99.44 (52)			Crystal
Fluorite				71.83			48.67				
	13	0.015 (18)	0.021 (35)	73.96 (33)	0.089 (88)	0.0042 (81)	48.98 (17)	102.44 (43)			Crystal

For each substance, the first row indicates theoretical amounts and the second row gives analysis by electron microprobe (*n* = number of analyzed points). Analytical totals are corrected for the fluorine-equivalent oxygen; elevated total values of cryolite and fluorite are related to the microprobe correction procedure and do not affect crystalochemical stoichiometries. Standard deviations are 1σ. Abbreviations: A/NK = molar $Al_2O_3/(Na_2O+K_2O)$, A/CNK = molar $Al_2O_3/(CaO+Na_2O+K_2O)$.

agate mortar, ground for 1 h under alcohol or acetone and dried overnight. The mixture was transferred to a platinum crucible and decarbonated at a heating rate of 150 °C/h followed by 8 h at 1020 °C. Melting was carried out in several cycles at 1400–1600 °C for 1 or 2 h, with intermittent crushing. Glass chips after each cycle were analyzed with an electron microprobe to monitor compositional homogeneity and alkali loss. Two to four melting cycles were used, depending on glass composition. The final glass was finely crushed and ground for 1 h in an agate mortar (dry) and stored at 120 °C until use. Glass compositions are presented in Table 1.

Fluorine dopings were calculated to have identical compositions as haplogranitic glasses, with F_2O_{-1} as the only variable (Table 2). These mixes were prepared by careful weighing of K_3AlF_6 (99%), Na_3AlF_6 (99.5%), topaz (Topaz Mountain, Utah) and SiO_2 (99.99%) into an agate mortar and grinding for 1 h (dry). This approach avoids any shifts in major oxide proportions and allows for saturation with any of these phases (e.g., cryolite or topaz) if conditions so arise. Calcium dopings were anorthite glass, wollastonite glass or crystalline $CaSiO_3$ powder (99.9%). Fluorite grains were cleaved fragments (2.5–4.4 mm^3) from a pale green, clear and inclusion-free, single crystal of fluorite (Jolynn mine, New Hampshire). Fluorite powder was derived from the same crystal by crushing, grinding and sieving to retain the fraction between 100 and 200 mesh. CaF_2 was reagent grade, finely

Table 2
Chemical composition of base mixes

Symbol	SiO_2 (wt.%)	Al_2O_3	CaO	Na_2O	K_2O	F	A/NK	A/CNK	Constituents
Single-grain dissolution experiments									
ALGA-05	75.922	14.895	1.008	3.620	4.555		1.369	1.171	ALG-12, an/gl
G12F-05	77.388	13.705		3.798	4.779	0.572	1.2	1.2	ALG-12, cr, kaf, tp, s
G12F-10	77.131	13.659		3.785	4.763	1.143	1.2	1.2	ALG-12, cr, kaf, tp, s
G12F-20	76.617	13.568		3.760	4.731	2.286	1.2	1.2	ALG-12, cr, kaf, tp, s
G12F-50	75.076	13.296		3.685	4.636	5.715	1.2	1.2	ALG-12, cr, kaf, tp, s
GA-05	77.652	12.974	1.008	3.705	4.662		1.164	1.0	HPG-2, an/gl
G1F-05	79.214	11.691		3.888	4.892	0.546	1.0	1.0	HPG-2, cr, kaf, tp, s
G1F-10	78.963	11.654		3.875	4.876	1.092	1.0	1.0	HPG-2, cr, kaf, tp, s
AKGA-05	76.330	12.779	1.008	5.304	4.580		0.934	0.824	AKG-8, an/gl
G8F-05	77.796	11.481		5.563	4.804	0.615	0.8	0.8	AKG-8, cr, kaf, tp, s
G8F-10	77.518	11.440		5.543	4.787	1.230	0.8	0.8	AKG-8, cr, kaf, tp, s
G8F-40	75.851	11.194		5.424	4.684	4.919	0.8	0.8	AKG-8, cr, kaf, tp, s
Powder experiments									
ALGF-03	75.315	13.338	2.155	3.696	4.651	1.460	1.2	0.887	ALG-8, fr/x
ALGF-05	73.762	13.063	3.591	3.620	4.555	2.433	1.2	0.750	ALG-12, fr/rg
ALGFF-1	73.637	13.041	3.232	3.614	4.547	3.333	1.2	0.779	ALGF-05, cr, kaf, tp, s
ALGFF-2	73.511	13.018	2.873	3.608	4.539	4.233	1.2	0.810	ALGF-05, cr, kaf, tp, s
ALGFF-5	73.134	12.952	1.796	3.589	4.516	6.932	1.2	0.921	ALGF-05, cr, kaf, tp, s
GAF-01	77.220	12.607	1.525	3.705	4.662	0.487	1.132	0.906	HPG-2, an/gl, fr/x
GF-02a	78.393	11.493	1.201	3.822	4.809	0.487	1.0	0.840	HPG-2, wo/x, fr/fg
GF-02b	78.393	11.493	1.201	3.822	4.809	0.487	1.0	0.840	HPG-2, wo/gl, fr/x
GF-01	78.671	11.610	0.718	3.861	4.858	0.487	1.0	0.899	HPG-2, fr/x
GF-03	77.081	11.376	2.155	3.783	4.760	1.460	1.0	0.744	HPG-2, fr/x
GFR-05	75.492	11.141	3.591	3.705	4.662	2.433	1.0	0.630	HPG-2, fr/rg
GFF-1	75.387	11.126	3.232	3.700	4.655	3.282	1.0	0.654	GFR-05, cr, kaf, tp, s
GFF-2	75.282	11.110	2.873	3.695	4.649	4.130	1.0	0.680	GFR-05, cr, kaf, tp, s
GFF-5	74.968	11.064	1.796	3.679	4.629	6.675	1.0	0.772	GFR-05, cr, kaf, tp, s
AKGF-05	74.170	10.946	3.951	5.304	4.580	2.433	0.8	0.542	AKG-8, fr/rg
AKGFF-2	73.839	10.897	2.873	5.280	4.560	4.406	0.8	0.578	AKGF-05, cr, kaf, tp, s
AKGFF-4	73.508	10.849	2.155	5.256	4.539	6.379	0.8	0.621	AKGF-05, cr, kaf, tp, s
AKGFF-5	73.343	10.824	1.796	5.244	4.529	7.365	0.8	0.644	AKGF-05, cr, kaf, tp, s
AKGF-03	75.732	11.177	2.155	5.415	4.677	1.460	0.8	0.625	AKG-8, fr/x

All compositions are normalized to 100 wt.%, including the fluorine-equivalent correction for oxygen. Abbreviations: A/NK = molar $Al_2O_3/(Na_2O+K_2O)$, A/CNK = molar $Al_2O_3/(CaO+Na_2O+K_2O)$, cr—crystalline cryolite, kaf—crystalline K_3AlF_6, tp—crystalline topaz, s—crystalline silica (quartz and tridymite mixture, Hudon et al., 2003), an/gl—anorthite glass, wo/gl—wollastonite glass, wo/x—crystalline $CaSiO_3$, fr/x—crystalline fluorite (100–200 mesh), fr/rg—reagent grade CaF_2, finely pulverized.

pulverized (Baker Analyzed). Individual starting compositions were prepared by weighing base glasses or mixes and grinding for 1 h in an agate mortar (dry). The weighed-in compositions of all base mixes are given in Table 2.

Experiments were performed in Au capsules with 2.0–2.2 mm OD (powder melting runs) and 3.0 mm OD (single-grain dissolution runs). 10-mm long capsules were cut from seamless tubing, washed in concentrated hydrofluoric acid, repeatedly rinsed in distilled water, cleaned with alcohol in an ultrasonic bath and annealed to yellow-orange color over a Meeker burner. For powder melting, capsules were crimped and welded flat, whereas for grain dissolution, capsules were crimped and welded with a trifold to create sufficient space for melt to completely surround the fluorite crystal. All experiments were performed with 10 wt.% H_2O, relative to the granite powder (i.e., excluding the fluorite crystal). Capsules were filled with distilled and deionized water (0.8–1.0 mg), fluorite crystal (8–14 mg, if necessary) and granitic powder (7.2–9.0 mg), and crimped and welded immediately. During welding, capsules were partly submerged in a cold water bath to prevent loss of H_2O. In all cases, weight loss during welding is 0.04–0.08 mg; random checks by piercing the welded capsule and determining the weight loss by drying revealed no loss of H_2O within the weighing error (0.02 mg). The weighed-in H_2O content is 10 ± 0.1 wt.%. Capsules were stored at 120 °C for 1 h to ensure homogeneous distribution of H_2O vapor and re-weighed to check for leakage.

Experiments were carried out in cold-seal pressure vessels (800 °C) and rapid-quench TZM pressure vessels (950 °C) at 100 MPa, using argon as pressure medium. Temperatures were monitored by external chromel-alumel thermocouples, calibrated against the melting point of NaCl (800.6 °C) and a factory-calibrated thermocouple. Individual temperatures are accurate to ±2 °C (cold-seal vessels) and ±5 °C (TZM vessels). Pressure was measured with the Bourdon-tube gauges, calibrated against a factory calibrated Heise gauge. Pressure data are accurate to ±5 MPa and precise to ±2 MPa. Cold-seal vessel experiments were terminated by placing the vessel in an air jet and quenched below the solidus temperature in 1–2 min. TZM vessel experiments were terminated by a free fall of the sample into the cooling collar with a quenching rate of ~100 °C/s. All capsules were checked for leakage, opened and stored at room conditions.

Attainment of equilibrium was verified by several means: varying the run duration (1 to 30 days), using different experimental designs (single-grain dissolution vs. powder melting) and using different starting materials (glasses vs. crystalline phases). The majority of the experiments were performed for 7 days and the results (final melt compositions) are mutually consistent among the above approaches; all equilibrium run results are reported in Tables 3 and 4). This is in agreement

Table 3
Experimental conditions and results (100 MPa, 10 wt.% H_2O)

Run	Mix	Temperature (°C)	Duration (h)	Assemblage
Grain-dissolution experiments				
443	HPG-2	800	726.1	L+fr+wo
444	AKG-8	800	726.1	L+fr
445	ALG-12	800	726.1	L+fr
493	HPG-2	800	26.8	L+fr+wo (rare)
494	ALG-12	800	26.8	L+fr
495	AKG-8	800	26.8	L+fr
618	ALGA-05	800	162.3	L+fr
619	G12F-05	800	162.3	L+fr
620	G12F-10	800	162.3	L+fr
621	G12F-20	800	162.3	L+fr
622	G12F-50	800	163.1	L+fr
623	AKGA-05	800	163.1	L+fr
624	G8F-05	800	163.1	L+fr
625	G8F-10	800	163.1	L+fr
626	G8F-40	800	166.8	L+fr
627	GA-05	800	166.8	L+fr
628	G1F-05	800	166.8	L+fr
629	G1F-10	800	166.8	L+fr
631	HPG-2	950	23.7	L+fr
632	ALG-12	950	23.7	L+fr
638	AKG-8	950	23.7	L+fr
Powder experiments				
360	GFR-05	800	170.3	L+fr
361	GFF-1	800	170.3	L+fr
362	GFF-2	800	170.3	L+fr
363	GFF-5	800	170.3	L+fr+qz
364	ALGF-05	800	169.8	L+fr
365	ALGFF-1	800	169.8	L+fr
366	ALGFF-2	800	169.8	L+fr
367	ALGFF-5	800	169.8	L+fr+qz
368	AKGF-05	800	169.8	L+fr
398	GFF-1	800	171.2	L+fr
399	ALGFF-1	800	171.2	L+fr
401	AKGFF-2	800	171.2	L+fr
402	AKGFF-5	800	171.2	L+fr+cry
433	AKGFF-4	800	175.2	L+fr
451	GF-01	800	163.5	L+fr
452	GF-02a	800	163.5	L+fr+wo
453	GF-02b	800	163.5	L+fr+wo
473	AKGF-03	800	175.3	L+fr
474	ALGF-03	800	175.3	L+fr
475	GAF-01	800	175.3	L+fr
476	GF-03	800	175.3	L+fr

All runs are fluid-saturated. Abbreviations: pw—powder-melting experiment, gr—grain-dissolution experiment, L—liquid, fr—fluorite, wo—wollastonite, qz—quartz, cry—cryolite.

Table 4
Composition of fluorite-saturated melts

Run	*n*	SiO_2 (wt.%)	Al_2O_3	CaO	Na_2O	K_2O	F	Total
Single-grain dissolution experiments								
443	30	72.78 (26)	11.052 (38)	0.5488 (93)	3.569 (32)	4.430 (43)	0.388 (10)	92.61 (27)
444	24	71.28 (28)	10.785 (53)	0.6661 (83)	5.112 (49)	4.338 (31)	0.511 (11)	92.48 (29)
445	34	70.93 (17)	12.717 (39)	1.3181 (72)	3.522 (38)	4.359 (35)	0.8683 (97)	93.35 (18)
493	18	73.77 (92)	11.54 (32)	0.539 (13)	3.659 (61)	4.486 (59)	0.3249 (97)	94.19 (98)
494	22	69.68 (78)	13.44 (33)	1.916 (12)	3.066 (54)	3.897 (54)	0.892 (25)	92.52 (85)
495	24	70.49 (24)	10.741 (52)	0.8014 (72)	5.121 (37)	4.291 (33)	0.4860 (95)	91.72 (25)
618	17	70.59 (59)	13.32 (49)	2.16 (26)	3.029 (92)	4.13 (13)	0.767 (26)	93.68 (82)
619	12	68.52 (45)	12.23 (14)	1.247 (16)	3.120 (56)	4.148 (78)	1.218 (34)	89.97 (48)
620	13	71.09 (45)	12.812 (91)	1.265 (14)	3.378 (58)	3.923 (62)	1.919 (33)	93.58 (46)
621	23	69.95 (33)	12.693 (76)	1.0262 (83)	3.338 (52)	4.032 (37)	2.857 (36)	92.70 (34)
622	18	66.07 (22)	12.690 (59)	1.1108 (98)	3.048 (36)	3.516 (41)	5.514 (59)	88.00 (24)
623	9	67.4 (1.6)	11.95 (29)	1.55 (17)	4.79 (30)	4.25 (12)	0.427 (48)	90.2 (1.6)
624	28	71.92 (26)	10.831 (48)	0.279 (10)	4.946 (45)	4.215 (41)	0.721 (12)	92.61 (27)
625	23	68.64 (56)	10.597 (47)	0.1232 (72)	4.593 (48)	4.065 (36)	1.246 (23)	88.74 (56)
626	15	68.48 (29)	10.557 (54)	0.0425 (98)	4.179 (44)	3.519 (44)	4.418 (81)	89.33 (30)
627	14	72.86 (45)	12.34 (11)	2.137 (15)	3.357 (39)	4.110 (61)	0.530 (14)	95.11 (47)
628	10	71.44 (55)	10.731 (39)	0.460 (16)	3.306 (72)	4.208 (43)	0.666 (25)	90.53 (56)
629	17	71.60 (39)	10.593 (58)	0.2461 (80)	3.158 (45)	4.436 (46)	1.017 (21)	90.62 (40)
630	17	71.97 (29)	10.802 (60)	0.7761 (88)	3.414 (33)	4.184 (86)	0.386 (15)	91.37 (31)
631	15	73.23 (24)	11.163 (85)	1.153 (78)	3.522 (47)	4.390 (38)	0.781 (53)[a]	93.51 (27)
632	21	69.27 (42)	12.608 (42)	2.532 (26)	3.381 (36)	4.178 (39)	1.506 (26)	92.84 (43)
638	17	69.50 (35)	10.300 (52)	1.984 (28)	4.893 (63)	4.267 (45)	1.245 (16)	91.67 (37)
Powder experiments								
360	6	71.80 (34)	10.72 (13)	0.477 (94)	3.363 (84)	4.420 (70)	0.314 (59)	90.97 (43)
361	4	71.4 (1.2)	10.54 (25)	0.52 (30)	3.187 (84)	4.122 (41)	1.12 (18)	90.4 (1.3)
362	5	71.1 (1.5)	10.67 (13)	0.178 (77)	3.08 (15)	3.992 (93)	1.96 (11)	90.1 (1.7)
363	8	69.0 (1.9)	11.01 (61)	0.238 (34)	3.19 (27)	3.51 (14)	5.27 (34)	90.0 (1.6)
364	4	68.7 (1.0)	12.41 (12)	1.140 (91)	3.214 (64)	4.311 (72)	0.696 (30)	90.2 (1.2)
365	6	68.58 (66)	12.34 (20)	1.30 (41)	3.16 (19)	4.06 (13)	1.65 (15)	90.40 (64)
366	11	68.31 (90)	12.34 (16)	0.755 (35)	2.97 (38)	3.76 (13)	2.576 (80)	89.6 (1.2)
367	13	65.7 (1.0)	12.57 (21)	0.970 (58)	2.89 (16)	3.274 (89)	5.98 (15)	88.83 (96)
368	5	69.29 (68)	10.42 (18)	0.584 (30)	4.52 (20)	4.20 (12)	0.426 (33)	89.27 (80)
398	6	70.83 (56)	10.75 (11)	0.117 (19)	3.09 (16)	4.08 (11)	1.107 (32)	89.50 (97)
399	10	69.25 (58)	12.55 (10)	0.846 (34)	3.224 (87)	4.079 (53)	1.582 (34)	90.86 (71)
401	5	70.21 (85)	10.881 (63)	0.044 (26)	4.868 (83)	3.96 (16)	2.60 (15)	91.46 (77)
402	15	68.37 (90)	11.40 (18)	0.0065 (57)	4.62 (19)	3.511 (87)	6.01 (26)	91.4 (1.2)
433	15	69.72 (57)	10.73 (11)	0.020 (13)	4.44 (16)	3.557 (93)	4.50 (16)	91.07 (73)
451	13	73.2 (1.1)	10.93 (14)	0.479 (20)	3.456 (68)	4.55 (19)	0.404 (26)	92.9 (1.3)
452	8	72.50 (58)	10.860 (82)	0.463 (18)	3.373 (56)	4.51 (12)	0.385 (40)	91.92 (65)
453	13	71.69 (78)	10.785 (70)	0.458 (28)	3.378 (88)	4.376 (82)	0.383 (48)	90.91 (84)
473	12	70.79 (97)	10.68 (12)	0.626 (28)	4.83 (18)	4.18 (13)	0.505 (29)	91.4 (1.3)
474	18	68.86 (61)	12.26 (12)	1.216 (46)	3.176 (86)	4.23 (14)	0.800 (47)	90.20 (69)
475	12	70.40 (42)	11.68 (18)	1.470 (27)	3.14 (37)	4.27 (16)	0.451 (22)	91.21 (66)
476	12	73.01 (88)	10.87 (13)	0.501 (23)	3.480 (99)	4.58 (13)	0.369 (25)	92.7 (1.1)

Analytical totals include the fluorine-equivalent correction of oxygen; *n* = number of analyzed points in diffusion profile(s). Standard deviations are 1σ.

[a] Calculated from CaO by CaF_2 stoichiometry.

with the estimated equilibrium time of 4 days for volatile-bearing granitic systems (Steiner et al., 1975; Candela and Holland, 1984; Williams et al., 1997; Frank et al., 2003).

Run products were studied petrographically in grain mounts and stable phases identified by electron microprobe. Glass chips (powder-melting runs) and whole capsules (crystal-dissolution runs) were mounted in plastic epoxy, ground and polished with SiC and Al_2O_3 powders in oil–ethanol mixtures, with intermittent ultrasonic cleaning with ethanol. Glass compositions were analyzed by the JEOL electron

microprobe at the following conditions: accelerating voltage 15 kV, beam current 5 nA and beam diameter 20 μm. Counting times were 100 s for F and Ca, and 20 s for other elements. Counting statistics in time-series measurements revealed no volatilization of Na and F at these conditions. The quality of calibration was monitored by periodically analyzing pure fluorite and topaz crystals. The reported data represent averages of multiple measurements and are reported with standard deviations as 1σ. Measurement errors were treated by standard error propagation laws (Bevington and Robinson, 1992).

For the single-grain dissolution experiments, the equilibrium concentrations (fluorite solubilities in the melt) were retrieved by analyzing diffusion profiles away from the crystal–melt interface. Element diffusion from an infinite planar source with time-independent concentration is described by the analytical solution to the Fick's law (Watson, 1991; Albarède, 1995):

$$\frac{c - c_0}{c_i - c_0} = erfc\left(\frac{x}{2\sqrt{Dt}}\right) \quad (4)$$

where x is a distance away from the crystal–melt interface, D is the diffusion coefficient, t is time (run duration), c is the time- and distance-dependent concentration of the element of interest in the melt (analyzed), c_i represents the initial concentration in the melt (concentration at the infinite distance from the interface), c_0 is the concentration at the fluorite crystal–melt interface (i.e., the equilibrium solubility) and erfc is the complementary error function (1 − erf). The diffusional profile, analyzed by the electron microprobe, is linearized (e.g., Harrison and Watson, 1983) and the $\mathrm{erfc}^{-1}\{(c-c_0)/(c_i-c_0)\}$ vs. x is fitted by the linear least-squares algorithm for variables with independent errors (Reed, 1989, 1992). Run durations of individual experiments were chosen to produce long diffusion distances which were measured over several hundred micrometers. This technique provides quasilinear composition profiles that accurately constrain equilibrium solubilities, c_0, at the expense of the diffusion coefficients, D, which are extraneous for our purpose. Representative diffusion profiles of calcium and fluorine concentrations in 1-day and 1-week experiments are shown in Fig. 2.

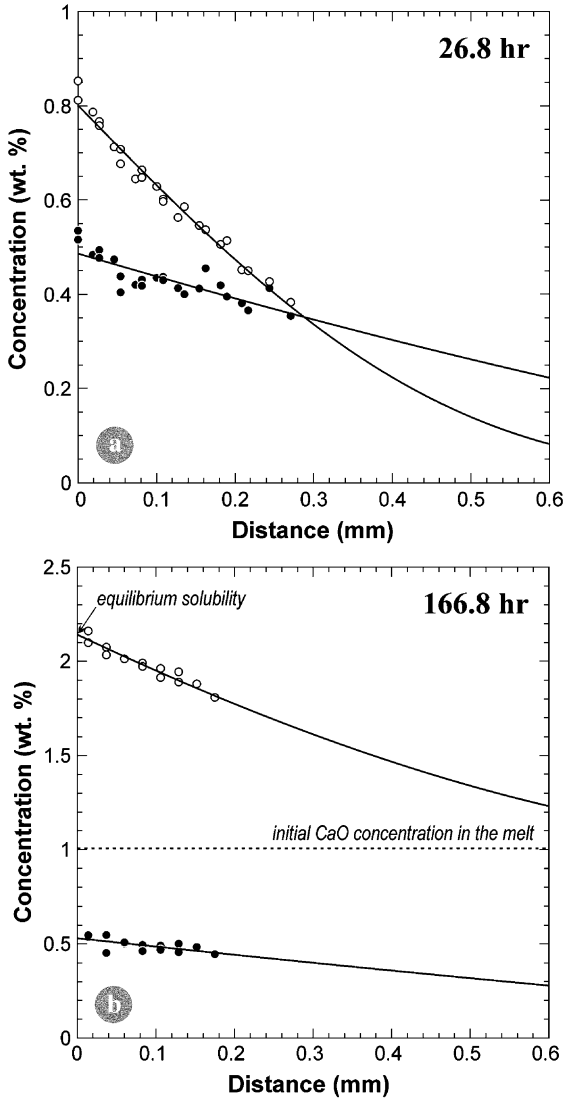

Fig. 2. Representative diffusion profiles for grain dissolution experiments: (a) run 495, (b) run 627. Point symbols are analytical points by electron microprobe: CaO (open circles) and F (solid circles). Solid curves are fits of the Fick's law (Eq. (4)) used to determine equilibrium fluorite solubility.

3. Results

We have performed 21 powder-melting experiments and 21 single-grain dissolution experiments in the system haplogranite–CaO–F_2O_{-1} with variable alumina saturation index, at 800–950 °C, 100 MPa and 10 wt.% H_2O. All runs were fluid- and fluorite-saturated and several experiments contained cryolite, wollastonite or quartz as additional solid phases (Table 3). As a consequence of the fluid saturation, small amounts of alkalies and Si partition to the aqueous fluid phase and therefore the molar $Al_2O_3/(Na_2O+K_2O+CaO)$ ratio of the melt rises slightly above the nominal (initial) values with increasing fluorine content in the system. We retain the nomenclature according to the initial compo-

sition (peralkaline, subaluminous and peraluminous) to distinguish individual experiment sets but all interpretations were performed with actual (analyzed) values of the aluminum and alkali concentrations.

Melts in experiments with the highest fluorine contents co-saturate with cryolite in peralkaline compositions (# 402) and with quartz in weakly to strongly peraluminous conditions (# 363 and 367; Table 3). Increased activity of quartz with increasing fluorine content results from the melt-speciation mechanism:

$$(\mathrm{Na,K})\mathrm{AlSi_3O_8(l)} + \mathrm{F_2O_{-1}} = (\mathrm{Na,K})\mathrm{AlF_4(l)} + 3\mathrm{SiO_2(l,s)} \quad (5)$$

where (Na,K)AlF_4 represents a tetrahedrally coordinated aluminofluoride complex (e.g., Schaller et al., 1992; Zeng and Stebbins, 2000). Thus, increasing concentration of fluorine in the melt decreases activity of alkali feldspar and promotes quartz saturation (cf. Wyllie and Tuttle, 1961; Manning, 1981; Kogarko and Krigman, 1981). None of the F-doped experiments reached saturation by topaz (despite its addition as a dopant) which implies that topaz solubility in subaluminous to peraluminous melts (ASI=1.00–1.25) is greater than 6 wt.% F (at 800 °C, 100 MPa and fluid saturation).

Experiments with elevated calcium concentrations were aimed at investigating the stability or metastability of wollastonite (Gabitov et al., 2001, R. Linnen, personal communication, 2001, Dolejš and Baker, 2001). The single-grain dissolution experiments along the granite (ASI=1)–fluorite join produce pseudobinary wollastonite (# 443, 1 day; # 493, 30 days, Table 3). Wollastonite occurs as individual subhedral elongate grains (7–12 μm) disseminated in the granitic melt within 25 μm from the fluorite–melt interface. On the other hand, wollastonite does not form in experiments with natural fluorite powder (# 451 and 476) or reagent-grade CaF_2 (# 360) at the same join and conditions. In order to locate the stable fluorite–wollastonite cotectic, additional experiments were performed with $CaSiO_3$ added in the crystalline and glass form (# 452 and 453). Both runs produced wollastonite and fluorite as stable solid phases, and the calcium and fluorine concentrations in the melt fall very close to the granite–fluorite binary (Table 4), i.e., CaF_2 stoichiometry (Fig. 3). These results reveal that wollastonite liquidus surface closely approaches the hydrous haplogranite–fluorite binary join at 800 °C and in the single-grain dissolution runs, wollastonite forms metastably in the time-dependent diffusional profile. The wollastonite stability field does not intersect the granite–fluorite join at and above 800 °C, 100 MPa and fluid saturation (cf. Table 3).

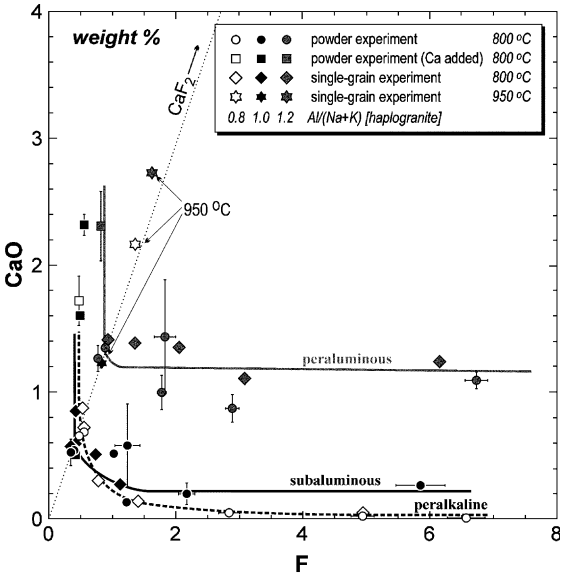

Fig. 3. CaO vs. F concentrations in run-product glasses (wt.%, on anhydrous basis) at fluorite saturation, 800–950 °C, 100 MPa and 10 wt.% H_2O in the system.

4. Fluorite solubility

Equilibrium concentrations of CaO and F in the fluorite-saturated melts are listed in Tables 4 and 5 and with the fluorite saturation isotherms presented in Fig. 3. On the hydrous haplogranite–fluorite join, fluorite solubilities are low: 1.05 (peralkaline), 0.82 (subaluminous) and 1.92 wt.% CaF_2 (peraluminous), at 800 °C, 100 MPa and H_2O saturation (Table 5). Thus, fluorite crystallization buffers concentrations of fluorine and/or calcium at very low levels. The values also indicate a solubility minimum near the subaluminous composition and more than a twofold increase of fluorite solubility in the peraluminous melts (ASI~1.2, Table 5).

The purpose of Ca- or F-doped experiments was to investigate the possible decoupling of CaO and F components and their interactions with excess alkalies or aluminum in melts with a variable alumina saturation index. For each set of experiments (peralkaline, subaluminous, peraluminous), the hyperbolic shape of the fluorite-saturation isotherms (Fig. 3) suggests that fluorite solubility is controlled by activities of CaO and F_2O_{-1} independently. The partial or complete decoupling of CaO and F_2O_{-1} structure indicates presence of other species in the melt structure, in addition to the Ca–F complexes (Weidner and Martin, 1987; Haapala, 1997; Tindle et al., 2002).

Table 5
Fluorite solubilities along the haplogranite–fluorite binary joins

	Peralkaline		Subaluminous		Peraluminous	
	wt.% CaF_2	Al/(Na+K), cat.	wt.% CaF_2	Al/(Na+K), cat.	wt.% CaF_2	Al/(Na+K), cat.
800 °C	1.054 (85)	0.824 (32)	0.822 (76)	1.036 (19)	1.92 (15)	1.219 (25)
950 °C	2.90 (16)	0.8130 (84)	1.71 (16)	1.058 (12)	3.57 (33)	1.2502 (99)

The data are results of weighted averages of multiple experiments (800 °C) or analyzed results of single experiments (950 °C). Solubilities are reported on anhydrous basis.

An asymptotic approach of the solubility isotherms to the concentration axes has the following implication: in a melt composition where one component is significantly more abundant than the other (i.e., molar F≫2Ca or 2Ca≫F), the fluorite crystallization is controlled by the less-abundant component and is essentially independent of the more-abundant component. Continuing cotectic fractionation of fluorite with rock-forming silicates will buffer the less-abundant component whereas the more-abundant component will increase or decrease in accordance with the overall liquid line of descent. In calc-alkaline and Ca-rich peralkaline magmatic suites, fluorite crystallization buffers fluorine concentration in the melt and the calcium abundance will follow the general fractionation trend dictated by precipitating silicate minerals. On the other hand, in F-rich granites (F≫Ca), the fluorite saturation depends on the CaO content in the melt and the fluorine concentration in the melt will continue to increase in the presence of fluorite.

Fig. 4 illustrates the fluorite solubility by the concentration of the "saturating" component as a function of melt aluminosity, expressed as $Al_2O_3^{exc} = Al_2O_3 - Na_2O - K_2O$ in moles per hundred anions on anhydrous basis. The values of $Al_2O_3^{exc}$ are positive for peraluminous compositions and negative for peralkaline compositions. The change in fluorite solubility with Ca-doping is insignificant (Fig. 4a). Using anorthite glass as a Ca-source results in no change in the fluorite solubility in peralkaline and peraluminous melts (# 623 and 618). The fluorite solubility in anorthite-doped subaluminous melts increases slightly (# 475 and 627), but remains considerably lower than in peraluminous melts. This means that excess portions of Ca and Al remain associated in anorthite-bearing melts. The fluorite solubility in wollastonite-doped subaluminous melts does not change (# 452 and 453) due to the saturation by solid wollastonite, which removes excess Ca from the melt (Figs. 3 and 4).

In the F-enriched compositions, fluorite solubilities expressed by the CaO concentrations (Fig. 4b) decrease in all melts, owing to the separate effects of CaO and F on fluorite crystallization. This provides support for the partially independent speciation of Ca and F in the melt structure. The systematic shifts towards higher $Al_2O_3^{exc}$ values in all three experiment sets are due to the increased alkali partitioning to the aqueous fluid, in the presence of fluorine.

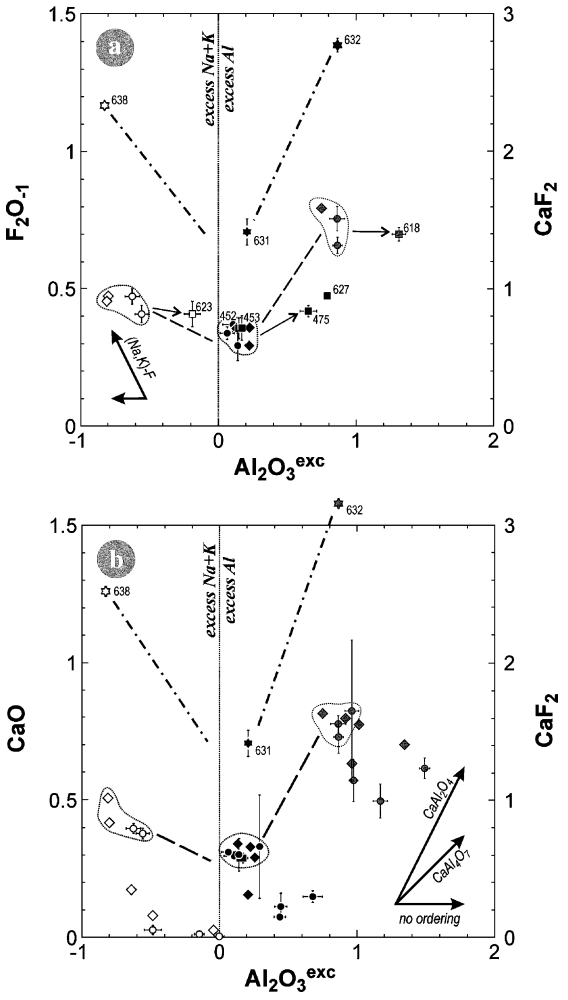

Fig. 4. Variations of fluorite solubilities with melt aluminosity, $Al_2O_3^{exc}$: (a) haplogranite–fluorite experiments (contoured areas) and Ca-doped experiments (squares); (b) haplogranite–fluorite experiments (contoured areas) and F-doped experiments. Vectors indicate shifts of fluorite solubility at alkali–F association (a) and Ca–Al association (b). Symbols are identical with those in Fig. 3.

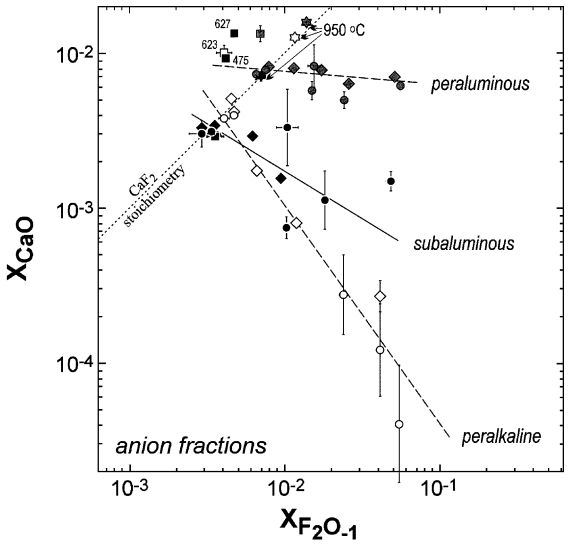

Fig. 5. CaO vs. F_2O_{-1} concentrations in run-product glasses (anion fraction) at fluorite saturation, 800–950 °C, 100 MPa and 10 wt.% H_2O in the system. Linear fits represent solubility isotherms (Eq. (7), Table 6). Symbols are identical with those in Fig. 3.

Compositions on the binary haplogranite–fluorite joins (Fig. 4, outlined areas) exhibit a minimum in fluorite solubility near the subaluminous composition ($Al_2O_3^{exc}=0$; cf. Scaillet and Macdonald, 2004). The increase in fluorite solubility in the peralkaline melts indicates that the excess alkalies are associated with fluorine (Fig. 4a), whereas the solubility increase in the peraluminous melts implies association between excess aluminum and calcium, as corroborated by results with anorthite-bearing melts (Fig. 4b).

5. Saturation isotherms and melt-speciation mechanisms

At both 800 and 950 °C, fluorite solubilities exhibit a minimum approximately at the subaluminous composition, cation Al/(Na+K)~1 (Table 5), which indicates different melt-speciation mechanisms in peralkaline vs. peraluminous systems.

The concentrations of CaO and F_2O_{-1} at fluorite saturation (Fig. 3) are regressed by the apparent equilibrium constant (e.g., Williams et al., 1997; Frank et al., 1998):

$$K = \frac{a(CaF_2)}{X(CaO)\cdot X(F_2O_{-1})^c} \quad (6)$$

by linear fitting in log $X(CaO)$ − log $X(F_2O_{-1})$ space, with the logarithmic equilibrium constant (log K) and the stoichiometric coefficient, c, as resulting parameters:

$$\log X(CaO) = -c\log X(F_2O_{-1}) - \log K. \quad (7)$$

Concentrations of CaO and F_2O_{-1} are expressed as anion fractions on anhydrous basis. Anion units are a suitable option for systems with F_2O_{-1} and have the advantage of barycentric behavior (mass conservation, Thompson, 1982; Spear, 1993), i.e., they facilitate CaO, F_2O_{-1} and CaF_2 conversions without re-normalizing concentrations of other components: $1CaO+1F_2O_{-1}=2Ca_{0.5}F$. The results are shown in Fig. 5, and parameters for the fluorite equilibrium constant at 800 °C are given in Table 6.

The fits include runs on the haplogranite–fluorite joins and F-doped runs. Experiments doped with $CaSiO_3$ precipitate the dopant as solid wollastonite and yield a fluorite solubility equivalent to the haplogranite–fluorite join; these runs were excluded to avoid the artificial weighting of the regression. Experiments doped with anorthite have, inevitably, higher melt aluminosity ($Al_2O_3^{exc}$ value); anorthite-enriched runs with subaluminous haplogranite (# 475 and 627) have resulting (actual) aluminosities very close to the peraluminous set. Additional regression including these runs with the peraluminous set yields a fit within error brackets of the original one (Table 6), thus the inclusion of the anorthite-doped experiments has an insignificant effect on the regression.

In order to calculate the isotherms as a function of melt aluminosity, the values of c and log K are related to the average value of $Al_2O_3^{exc}$ for each data set. In this way, all quantities, CaO, F_2O_{-1} and $Al_2O_3^{exc}$, are uni-

Table 6
Parameters for the apparent equilibrium constant at 800 °C, 100 MPa and H_2O saturation

Set	c	log K	$Al_2O_3^{exc}$	Runs
Peralkaline	1.41 (14)	5.79 (30)	−0.35 (27)	401, 402, 433, 473, 624–626
Subaluminous	0.61 (25)	3.99 (54)	0.34 (20)	361–363, 398, 476, 628–629
Peraluminous	0.085 (57)	2.287 (91)	1.08 (21)	365–367, 399, 474, 619–622
Peraluminous[a]	0.140 (48)	2.370 (80)	1.01 (24)	365–367, 399, 474–475, 619–622, 627

Multiple runs on the haplogranite–fluorite joins were excluded to avoid artificial weighting of the fits.
[a] Includes anorthite-doped experiments with the same $Al_2O_3^{exc}$ values (#475 and 627).

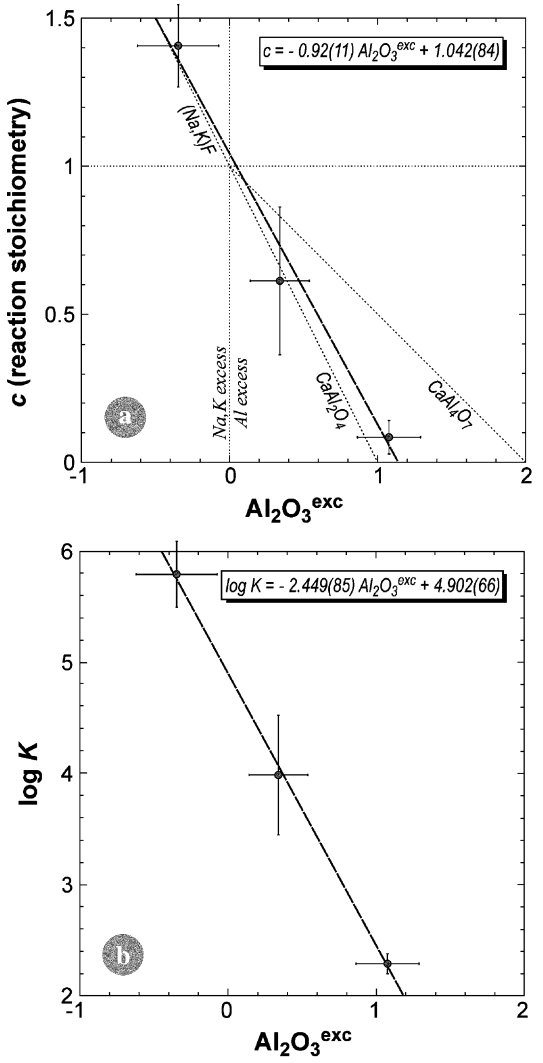

Fig. 6. Linear dependence of the stoichiometric parameter (c, Eq. (6)) and the apparent equilibrium constant (log K, Eq. (7)) on the melt aluminosity, $Al_2O_3^{exc}$ (Table 6). Dotted trends in (a) represent the limiting cases of complete (Na,K)–F and complete Ca–Al association, respectively.

formly expressed in molar amounts, are easily related to interaction stoichiometries (i.e., c in Eq. (6)), and thus supercede the non-linear behavior of the alumina saturation index which was used previously (Gabitov et al., 2001; Scaillet and Macdonald, 2004). The linear dependence of c and log K on $Al_2O_3^{exc}$ (Fig. 6) allows calculation of the isotherm parameters as function of melt aluminosity:

$$c = -0.92(11)Al_2O_3^{exc} + 1.042(84) \quad (8)$$

and

$$\log K = -2.449(85)Al_2O_3^{exc} + 4.902(66). \quad (9)$$

The variations of the stoichiometric parameter, c, have important implications for speciation mechanisms of calcium and fluorine in the melt structure. Since

$$CaO + F_2O_{-1} = CaF_2 \quad (10)$$

the departures of the stoichiometric parameter, c (Eq. (6)), from unity indicate partial association of CaO or F_2O_{-1} with other melt components. Where $c<1$, CaO enters the fluorite equilibrium (Eq. (10)) in excess over F_2O_{-1} and the CaO^{exc} must associate with oxyanions (e.g., silicate or aluminate tetrahedra). For $c>1$, F_2O_{-1} is present in excess and it partly associates with other cations (i.e., alkalies). In both cases, the fluorite solubility must increase due to the lower activity of one of its components.

The change of the reaction stoichiometry ($c=1$) occurs at $Al_2O_3^{exc}=0.046$ (91), i.e., at the subaluminous composition ($Al_2O_3^{exc}=0$) within error bracket (Fig. 6). This suggests the role of excess aluminum or excess alkalies in individual mechanisms. The possible stoichiometry of alkali–F or calcium–aluminum complexes is provided by the slope, $dc/d(Al_2O_3^{exc}) = -0.92 \pm 0.11$ (Eq. (8)), which is essentially negative unity, i.e., $CaO/Al_2O_3=1$ and $(Na,K)_2O/F_2O_{-1}=1$ in the complexes. Therefore, the following homogeneous melt-interaction mechanisms are applicable:

$$(Na,K)_2O + F_2O_{-1} = 2(Na,K)F \text{(in peralkaline compositions)} \quad (11)$$

$$CaO + Al_2O_3 = CaAl_2O_4 \text{(in peraluminous compositions)} \quad (12)$$

Abbreviating excess moles of alkali oxides or alumina, respectively, as a, the combination of Eq. (10) with (11), and Eq. (10) with (12) gives the overall reaction mechanisms:

$$CaO + (1+a)F_2O_{-1} + a(Na,K)_2O = CaF_2 + 2a(Na,K)F \text{(in peralkaline compositions)} \quad (13)$$

$$(1+a)CaO + F_2O_{-1} + aAl_2O_3 = CaF_2 + aCaAl_2O_4 \text{(in peraluminous compositions)} \quad (14)$$

In the latter case, the equilibrium can alternatively include SiO_2 and $CaAl_2Si_2O_8$ as quasicrystalline components (Burnham and Nekvasil, 1986; Burnham, 1992, 1997) with the same stoichiometric effect. Note that these overall stoichiometries pass through the error brackets of all three data sets in Fig. 6.

The alkali–F and Ca–aluminate complexing when excess alkalies or aluminum are present, in addition to Ca–F bonds, is a predictable consequence of variable cation field strength and anion polarizability. In peralkaline melts, weakly polarizable fluorine atoms preferentially bond to excess alkalies, rather than calcium, due to the lower field strength of alkalies. This short-range order is predicted by the nearly identical values for the Lewis basicity of NaF and haplogranitic glass (Duffy, 1989); on the basis of spectroscopic evidence, alkali–F bonds predominate in fluorine-bearing aluminosilicate glasses (Stebbins and Zeng, 2000; Zeng and Stebbins, 2000). In peraluminous melts, the effect is opposite, wherein excess Al_2O_3 bonds with network-modifying Ca to form stable calcioaluminate tetrahedra, $CaAl_2O_4$, found experimentally in fluorine-free glasses (Seifert et al., 1982; Hannon and Parker, 2000).

The presence of these species in the melt structure does not disqualify the existence of other complexes, which do not have a direct effect on the fluorite solution mechanisms, e.g., $(Na,K)AlF_4$ (Schaller et al., 1992; Stebbins and Zeng, 2000). However, the existence of the minimum in the fluorite solubility at the subaluminous composition together with observed increase of solubility in fluorine-doped peraluminous melts do not support the existence of the Al–F species in the melt.

6. Temperature dependence of fluorite solubility

Experiments on the haplogranite–fluorite joins were extended to 950 °C, 100 MPa and H_2O saturation in order to describe the temperature dependence of fluorite solubility as well as to gain further insights into fluoride–silicate interactions in the melt structure. The fluorite solubility increases with temperature in all compositions studied (Table 5). This increase, compared to solubilities at 800 °C, is approximately threefold (peralkaline composition) or twofold (subaluminous and peraluminous compositions). The absolute values are from 1.7 to 3.6 wt.% CaF_2 and imply that the buffered concentrations of fluorine remain within 0.8–1.7 wt.% F.

The temperature dependence of fluorite solubility in all three compositions has been compared to the liquidus depression, expressed by the cryoscopic equation (Schröder, 1893; Hildebrand and Scott, 1964):

$$-RT\ln a^{\mathrm{liq}} = \Delta H_{\mathrm{m}} + \int_{T_{\mathrm{m}}}^{T} \Delta c_{\mathrm{m}}\,\mathrm{d}T - T\left(\Delta S_{\mathrm{m}} + \int_{T_{\mathrm{m}}}^{T} \frac{\Delta c_{\mathrm{m}}}{T}\,\mathrm{d}T\right), \quad (15)$$

where a^{liq} is the ideal-mixing activity (concentration) of the dissolved component, ΔH_{m}, ΔS_{m} and Δc_{m} represent enthalpy, entropy and heat capacity of melting, respectively, and T_{m} is the fluorite melting temperature. Owing to the first-order transition between α- and β-CaF_2 at 1151 °C (0.1 MPa, Chase, 1998), it is necessary to derive hypothetical (metastable) thermochemical data for melting of α-CaF_2, applicable at 800–950 °C: ΔH_{m}=34551.7 J/mol, Δc_{m}=0 J/mol K (Mediaas et al., 2001), ΔV_{m}~0 J/mol bar (Hara and Ogino, 1981; Roberts and White, 1986; Tsytsenko et al., 1993; Jingu et al., 2002) and T_{m}=1645 K. The entropy of melting is calculated as: $\Delta S_{\mathrm{m}} = \Delta H_{\mathrm{m}} / T_{\mathrm{m}}$.

It must be noted that direct use of these values implies an assumption of mixing multiplicity corresponding to the stoichiometry, i.e., 1 mol CaF_2 standard state. In reality, fluoride species can substitute in the silicate framework as single anions (O vs. F, cf. Dolejš and Baker, 2004b), as polyhedral species on one network-former basis (e.g., aluminosilicate tetrahedra and fluoride polyhedra) or isovolumetrically as polycrystalline species (e.g., Si_4O_8, $NaAlSi_3O_8$, Ca_4F_8, etc., Burnham, 1981, 1994, 1997, Holland and Powell, 2001; Kirschen and Pichavant, 2001). These mixing mechanisms differ by multiples or fractions of configurational properties and have a strong effect on the resulting solubility of fluorite. For example, the configurational entropy in the single-anion mixing becomes eight times larger than in the Burnham quasicrystalline model. We will consider these mechanisms as two alternative and limiting cases for the temperature dependence of fluorite solubility.

A symmetric Margules (regular) formalism (Margules, 1895; Hildebrand, 1929; Anderson and Crerar, 1993; Powell and Holland, 1993) is sufficient for the thermodynamic description of the multicomponent silicate melts (Ghiorso et al., 1983, 2003; Holland and Powell, 2001; White et al., 2001). Eq. (15) is expanded to incorporate the non-ideal interaction term and rearranged:

$$T = \frac{\Delta H_{\mathrm{m}} + \Delta V_{\mathrm{m}}(p-1) + (1-x)^2 W}{\Delta S_{\mathrm{m}} - R\ln x}, \quad (16)$$

where x is an arbitrary liquid composition (mole or anion fraction), T is the corresponding liquidus temperature, p is pressure, W is the Margules interaction parameter and R is the universal gas constant, 8.31447 J/mol K (Mohr and Taylor, 2000). With increasing positive deviation from ideal mixing, the fluo-

rite liquidus will be intersected by the fluoride–silicate liquid–liquid immiscibility. The condition for the occurrence of stable (supraliquidus) immiscibility is $T_c > T$ ($x = 0.5$) where the consolute temperature, T_c, is calculated as follows (Prigogine and Defay, 1954; Guggenheim, 1967):

$$T_c = \frac{W}{2R}. \quad (17)$$

For conjugate immiscible liquids, the chemical potentials of corresponding end-member components are equal in both liquids; owing to the compositional symmetry, we use directly (Prigogine and Defay, 1954; Guggenheim, 1967):

$$T = 2T_c \frac{1-2x}{\ln\{(1-x)/x\}} \quad (18)$$

where x is an arbitrary solvus composition (mole or anion fraction), T is temperature (K), and the conjugate solvus composition is $1-x$. The calculated miscibility gaps produced by positive deviations from non-ideal mixing are shown in Fig. 7. This plot in the $\ln x$ vs. $1/T$ coordinates facilitates comparison of the liquid–liquid immiscibility, experimentally determined fluorite solubilities and allows separation of enthalpic and entropic effects on the solubility trends.

The overall low fluorite solubilities reflect either low configurational energies, i.e., small mixing multiplicities, or large positive deviations from ideal mixing. In Fig. 7a, experimental solubilities are compared to the calculated solubilities (Eq. (16)), by using the eight-anion mixing in the Burnham quasicrystalline formulation (Ca_4F_8, Burnham, 1997). The experimental data are within ~10 kJ of the ideal mixing, but the analyzed solubilities would require significant temperature dependences for the interaction parameter with progressively greater positive deviations at high temperatures. The original assumption of isovolumetric mixing on the eight-anion basis (Burnham, 1975, 1981, 1994) implies configurational entropy of the mixing of quadruplets of aluminosilicate tetrahedra (e.g., Si_4O_8, $[NaAl]_1Si_3O_8$), whereas experimental evidence suggests mixing of individual aluminate and silicate tetrahedra in F-free aluminosilicate melts (Flood and Knapp, 1968; Navrotsky et al., 1982; Ryerson, 1985). In the F-bearing systems, the incorporation of fluorine by interaction with bridging oxygens (Rabinovich, 1983; Mysen and Virgo, 1985) implies additional configurational contributions resulting from the oxygen–fluorine substitutions (cf. Luth, 1988; Dolejš and Baker, 2004b).

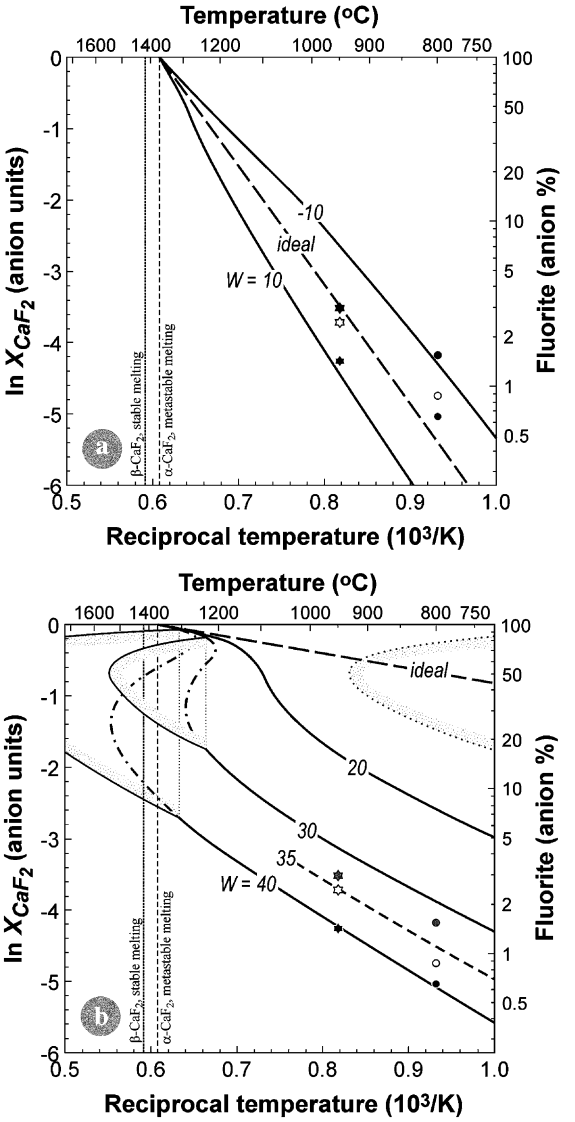

Fig. 7. Temperature dependence of fluorite solubility in the non-ideal fluorite–hydrous haplogranite binary system: (a) Burnham eight-anion mixing model (Burnham, 1981, 1994, 1997), (b) single-anion mixing model (fluorine per oxygen). W is the Margules interaction parameter in kJ. Miscibility gaps are stable (solid outlines, $W = 40$, 30 kJ) or metastable (dotted outline, $W = 20$ kJ). Symbols are identical with those in Fig. 3.

Fig. 7b presents results of the single-anion mixing model on the fluorine-per-oxygen basis. The experimental data fall within 32 to 40 kJ for W and the temperature dependence of data pairs are in good agreement with calculated trends of fluorite solubilities. Individual Margules interaction parameters for the hydrous haplogranite–fluorite binary are as follows: 36.0 ± 1.4 kJ (peralkaline), 39.7 ± 0.5 kJ (subaluminous) and 32.8 ± 0.7 kJ (peraluminous).

The trends of equilibrium solubilities can be recast to enthalpic and entropic contributions:

$$\ln x = -\frac{\Delta H}{R}\frac{1}{T} + \frac{\Delta S}{R} \quad (19)$$

The fluorite solubilities calculated by the non-ideal mixing models exhibit very similar d(ln x)/d(1/T) slopes at variable interaction parameters, W, in the low-temperature range (below 1000 °C, Fig. 6). However, the d(ln x)/d(1/T) slopes differ remarkably in each mixing model (Fig. 6a vs. b). That is, the enthalpic portion of the fluorite solubility is directly related to the mixing multiplicity. On the other hand, variations in degree of non-ideality (W) produce systematic changes in fluorite solubility, i.e., the entropic portion of the fluorite solubility is related to the non-ideal Margules parameter. The temperature trends of the data points (Fig. 7b) lend further support to the oxygen–fluorine anion mixing model for the F-bearing aluminosilicate melts, in contrast to the eight-anion quasicrystalline formulation (Burnham, 1981, 1997).

The positive deviations from ideal mixing will lead to the occurrence of the high-temperature fluoride–silicate liquid–liquid immiscibility. The monotectic temperatures are 1231 and 1303 °C at W=30 and 40 kJ, respectively. The prediction of the fluoride–silicate immiscibility, by the single-anion mixing model, is in agreement with experimental observations in the SiO_2–Al_2O_3–CaO–CaF_2 system (Hillert, 1964; Mukerji, 1965; Ueda and Maeda, 1999) and in the CaF_2-bearing aluminosilicate systems (Webster et al., 1998).

7. Calculation of fluorite solubility in hydrous silicic melts

We illustrate application of the present model by presenting procedure for calculating fluorite solubility and saturation isotherms in the multicomponent space. The model is pressure-independent ($\Delta V_m \sim 0$), but it has been calibrated at 100 MPa and H_2O saturation. In the first step, the whole-rock composition is converted to anion percent on an anhydrous basis (Thompson, 1982; Spear, 1993). Alumina excess or deficiency over alkali oxides is calculated as follows:

$$\begin{aligned} Al_2O_3^{exc} &= Al_2O_3 - Na_2O - K_2O \text{ (mol)} \\ &= (1/3)Al_{2/3}O - Na_2O - K_2O \text{ (anion\%)} \end{aligned} \quad (20)$$

The value of $Al_2O_3^{exc}$ is positive for peraluminous and metaluminous compositions and negative for peralkaline compositions, respectively. In the second step, the Margules interaction parameter, W (kJ), is calculated as a function of alumina balance:

$$W = 41.033 - 9.5498\ Al_2O_3^{exc} \left(Al_2O_3^{exc} \geq 0\right) \quad (21)$$

$$W = 41.033 + 6.8895\ Al_2O_3^{exc} \left(Al_2O_3^{exc} \leq 0\right) \quad (22)$$

In the third step, we iteratively solve the cryoscopic equation for the anion fraction of fluorite ($Ca_{0.5}F$), x_{fr}, at temperature of interest, T (K):

$$\begin{aligned} 0 = {} & \Delta H_m(1 - T/T_m) + \Delta V_m(p-1) + RT\ln x_{fr} \\ & + (1 - x_{fr})^2 W \end{aligned} \quad (23)$$

by using $\Delta H_m = 0.5 \cdot 34551.7$ J/mol ($Ca_{0.5}F$), $\Delta V_m = 0$ J/mol bar, $T_m = 1645$ K and $R = 8.31447$ J/mol K (see above, for references). The value of x_{fr} gives fluorite solubility on the haplogranite–CaF_2 join (cf. Fig. 4) and can be converted to anion % or wt.%. In order to calculate fluorite saturation isotherms in the CaO–F_2O_{-1} (or F) space (Fig. 3), two additional steps are necessary. Stoichiometric parameter of the fluorite solubility product (Eq. (6), Fig. 5) must be calculated as a function of alumina balance, and the effect of temperature must be incorporated in fluorite solubility (Eq. (16)). We assume that the melt interaction mechanisms, i.e., Ca–F, Ca–Al or alkali–F complexing, are temperature-independent as a first approximation. The relationship for a fluorite-liquidus isotherm is provided by Eq. (7) where c is calculated from Eq. (8) (Fig. 6a). On the haplogranite–CaF_2 join, molar or anion amounts of CaO and F_2O_{-1} are identical (congruent dissolution of fluorite) and related to fluorite solubility, x_{fr}, as follows:

$$x_{CaO} = x_{F_2O_{-1}} = 0.5\,x_{fr} \quad (24)$$

due to the mass-conservation principle of the anion units. By substituting Eq. (24) into Eq. (7), the fluorite-saturation isotherm provides the solubility product, K, at the temperature of interest:

$$K = \frac{1}{(0.5x_{fr})^{c+1}} \quad (25)$$

The values of c (Eq. (8)) and K (Eq. (25)) are parameters of the fluorite-saturation isotherm for the whole-rock composition and temperature of interest. The concentrations (anion fractions) of CaO and F_2O_{-1} (dependent and independent variable, respectively) calculated by Eq. (7) can be converted, for example, to weight percent. Since the fluorite dissolution causes minor shifts in proportions of other components and slightly decreases the alumina balance (due to

the dilution effect), the whole calculation procedure can be repeated with CaO and F_2O_{-1} from the previous step in order to obtain accurate results.

In order to demonstrate capabilities of the present model and to provide comparison with previous formulation of fluorite solubility by Scaillet and Macdonald (2004), we have calculated conditions for fluorite crystallization in a moderately peralkaline rhyolitic obsidian from Olkaria, Kenya Rift Valley (Marshall et al., 1998; Scaillet and Macdonald, 2001). Fig. 8 illustrates liquidus isotherms of fluorite in the temperature range of 500–1000 °C, calculated for matrix glass of the Olkaria obsidian (SMN 49; Scaillet and Macdonald, 2001). In the approach of Scaillet and Macdonald (2004) the model parameters are temperature and the Al/(Na+K) cation ratio, but their formulation ignores the effect of calcium, i.e., the fluorite liquidus isotherms are vertical (Fig. 8). The fluorite crystallization temperature is 562 °C which is ~100 °C lower than the pre-eruptive temperature (660 °C) constrained by the phase-equilibrium experiments (Scaillet and Macdonald, 2004). This has lead the authors to speculate about fluorine loss during eruption or poor quality of analytical results. In the present study, we consider effects of melt aluminosity, calcium content and temperature separately. The fluorite liquidus isotherms define hyperbolic trends in close agreement with experimental data points (Fig. 3) and predict fluorite crystallization temperature of 666 °C, in excellent agreement with the above phase-equilibrium constraints (Scaillet and Macdonald, 2001, 2003). The independent treatment of CaO and F concentrations appears not only to successfully reproduce the eruption temperature, but may eliminate large temperature errors (~80 °C) of the previous model and/or the need for syn-eruptive or post-solidification mobility of fluorine and/or alkalies (cf. Scaillet and Macdonald, 2004).

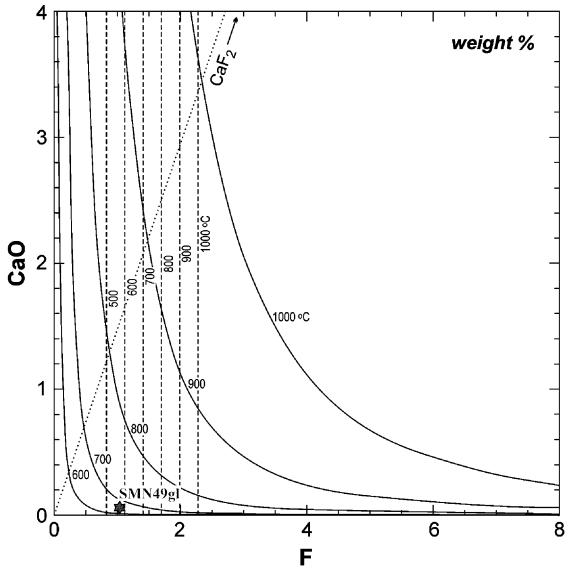

Fig. 8. Fluorite solubility in a peralkaline rhyolite obsidian glass from Olkaria, Kenya Rift valley (SMN49gl; Marshall et al., 1998; Scaillet and Macdonald, 2001). The saturation isotherms are calculated for the matrix glass composition (Scaillet and Macdonald, 2001) indicated by gray asterisk. Symbols: dashed lines—solubility model of Scaillet and Macdonald (2004), solid curves—present study (see text for discussion).

8. Fluorite stability in natural multicomponent systems

In natural multicomponent systems, the presence of additional oxide components (e.g., MgO, FeO, TiO_2, P_2O_5) affects the calcium speciation in the melt structure (i.e., activity of CaO) and the crystallizing rock-forming silicates and oxides define buffers which direct crystallization paths of liquids, as well as the stability of fluorine-bearing minerals through the corresponding chemical potentials. In order to compare stabilities of fluorite, topaz and cryolite and to illustrate relative levels of fluorine enrichment in natural systems, we use a chemical-potential space with independent components CaO and F_2O_{-1} (cf. Dolejš and Baker, 2004a). This space is limited by the fluorite saturation surface:

$$[\mathrm{CaO}] + [\mathrm{F_2O_{-1}}] = \mathrm{CaF_2(fluorite)} \qquad (26)$$

The stoichiometry of this equilibrium implies the reciprocal control of CaO and F_2O_{-1} on fluorite stability. Consequently, high-Ca suites will saturate with fluorite early and its presence will buffer fluorine concentration in the system at low levels. On the other hand, low-Ca systems will experience late fluorite saturation, after the fluorine enrichment. This thermodynamic treatment is in agreement with the present experimental results.

In calc-alkaline suites, rock-forming Ca-bearing silicate and oxide minerals define numerous buffers of μ(CaO) which subdivide the chemical-potential space (cf. Barton, 1996; Price et al., 1999; Dolejš and Baker, 2004a). Each univariant equilibrium reaches the fluorite saturation surface and defines an invariant point where μ(CaO) and $\mu(F_2O_{-1})$ are fixed (Fig. 9). These invariant points represent the maximum limit of fluorine enrichment, buffered by fluoride–silicate(–oxide) assemblages (for conversion between $\mu(F_2O_{-1})$ and fluorine concentration in the aqueous fluid or silicate melt, see Dolejš and Baker, 2004a). Owing to the

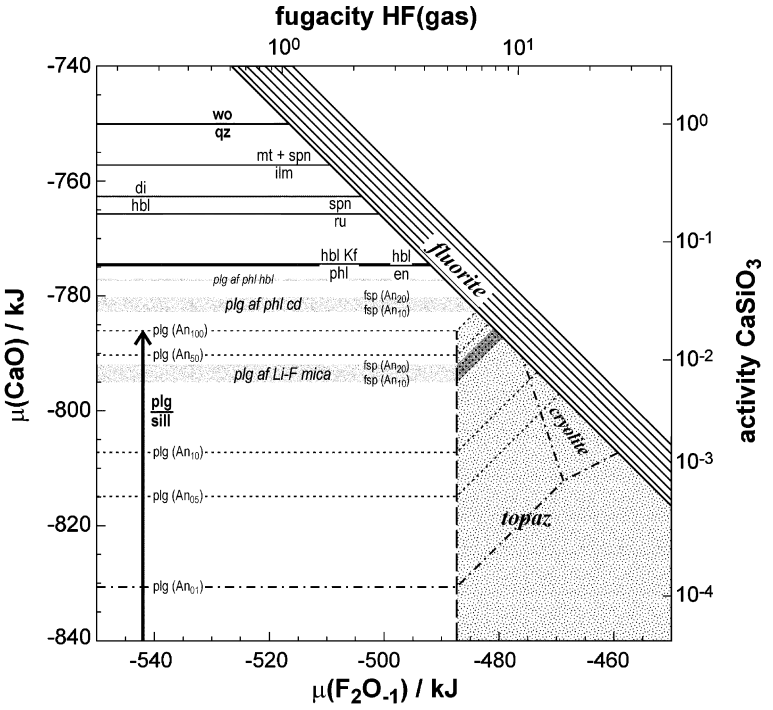

Fig. 9. μ(CaO) vs. $\mu(F_2O_{-1})$ chemical-potential diagram at 800 °C, 100 MPa and aqueous-fluid saturation. Individual silicate–oxide buffers, listed in Eqs. (26)–(35), subdivide the μ(CaO) space and allow comparison of common mineral assemblages. Relative levels of fluorine solubility are controlled by the slope of the fluorite saturation surface and increase from Ca-rich towards Ca-poor (peraluminous) compositions. Granites with Al_2SiO_5 polymorphs or Li–F–micas intersect the stability field of topaz. Thermodynamic data sources and solution models: Holland and Powell (1998), Dolejš and Baker (2004a), Fuhrman and Lindsley (1988), Wen and Nekvasil (1994), Dale et al. (2000); HF(gas) fugacity was calculated by the corresponding states formulation of the Compensated Redlich-Kwong equation (Holland and Powell, 1991) with critical data of Franck and Spalthoff (1957).

negative slope of the fluorite-saturation equilibrium (Eq. (26)), the buffered concentrations of fluorine increase progressively in the following sequence of fluorite–oxide–silicate buffers (Fig. 9):

$$6[\mathrm{CaO}] + 6\mathrm{FeTiO_3(ilmenite)} + 6\mathrm{SiO_2(quartz)} + \mathrm{O_2} = 6\mathrm{CaTiSiO_5(titanite)} + 2\mathrm{Fe_3O_4(magnetite)} \quad (27)$$

$$3[\mathrm{CaO}] + \mathrm{Ca_2Mg_5Si_8O_{22}(OH)_2(amphibole)} + 2\mathrm{SiO_2(quartz)} = 5\mathrm{CaMgSi_2O_6(clinopyroxene)} + \mathrm{H_2O} \quad (28)$$

$$[\mathrm{CaO}] + \mathrm{TiO_2(rutile)} + \mathrm{SiO_2(quartz)} = \mathrm{CaTiSiO_5(titanite)} \quad (29)$$

$$6[\mathrm{CaO}] + 5\mathrm{KMg_3AlSi_3O_{10}(OH)_2(biotite)} + 24\mathrm{SiO_2(quartz)} = 3\mathrm{Ca_2Mg_5Si_8O_{22}(OH)_2(amphibole)} + 5\mathrm{KAlSi_3O_8(feldspar)} + 2\mathrm{H_2O} \quad (30)$$

$$2[\mathrm{CaO}] + 5\mathrm{MgSiO_3(orthopyroxene)} + 3\mathrm{SiO_2(quartz)} + \mathrm{H_2O} = \mathrm{Ca_2Mg_5Si_8O_{22}(OH)_2(amphibole)} \quad (31)$$

All these equilibria reach the fluorite saturation surface and the buffered concentrations of fluorine will increase in the following sequence of mafic-mineral assemblages: magnetite–titanite<clinopyroxene< amphibole<rutile<biotite<orthopyroxene.

For Ca-poor peraluminous suites, the CaO–F_2O_{-1} chemical-potential space contains additional fluorine-bearing phases, topaz and cryolite, which may restrict fluorite stability and have cotectic or peritectic relationships. Individual equilibria occur with increasing $\mu(F_2O_{-1})$ as follows:

$$6[\mathrm{CaO}] + 2\mathrm{KAlSi_3O_8(alkali\ feldspar)} + 3\mathrm{Mg_2Al_4Si_5O_{18}(cordierite)} + 2\mathrm{H\pm_2O} = 6\mathrm{CaAl_2Si_2O_8(plagioclase)} + 2\mathrm{KMg_3AlSi_3O_{10}(OH)_2(biotite)} + 3\mathrm{SiO_2(quartz)} \quad (32)$$

$$[\mathrm{CaO}] + \mathrm{KAl_3Si_3O_{10}(OH)_2(white\ mica)} + 2\mathrm{SiO_2(quartz)} = \mathrm{CaAl_2Si_2O_8(plagioclase)} + \mathrm{KAlSi_3O_8(alkali\ feldspar)} + \mathrm{H_2O} \quad (33)$$

$$[CaO] + Al_2SiO_5(\text{sillimanite}) + SiO_2(\text{quartz}) = CaAl_2Si_2O_8(\text{feldspar}) \quad (34)$$

Fig. 9 illustrates that biotite granites crystallize with fluorite whereas sillimanite (andalusite) or Li–F–mica granites intersect stability fields of topaz and cryolite. The stability and sequence of formation of fluorine-bearing minerals during magmatic differentiation depends on the variance of the solid–liquid equilibria. With progressive fractionation of rock-forming silicates, magmas evolve along silicate(–oxide) buffers (Fig. 9, horizontal trends) towards higher $\mu(F_2O_{-1})$: (1) sillimanite- and andalusite-bearing granitic assemblages reach the topaz stability field at $\mu(F_2O_{-1}) = -487.4$ kJ (Fig. 9) and the coexistence of the Al_2SiO_5 polymorph and topaz invariantly buffers F_2O_{-1}:

$$[F_2O_{-1}] + Al_2SiO_5(\text{sillimanite, andalusite}) = Al_2SiO_4F_2(\text{topaz}) \quad (35)$$

The stability fields of cryolite and fluorite remain inaccessible, thus fluorite is not compatible with sillimanite or andalusite; (2) Li–F–mica granites reach the topaz field at $\mu(F_2O_{-1}) = -487.4$ kJ as well, but white micas do not buffer $\mu(F_2O_{-1})$ invariantly owing to their solid solution (Monier and Robert, 1986; Tischendorf et al., 2001). The progressive fractionation can proceed through the topaz field along the plagioclase–topaz univariant boundaries (Fig. 9, dotted lines) with concomitant changes in white-mica composition (e.g., towards lepidolite, Tindle and Webb, 1990, Tischendorf et al., 1997) and reach fluorite saturation. These relationships do not require phase removal by peritectic transitions, and all solid phases are expected to coexist in a cotectic manner.

In summary, fluorite is predicted to be stable in titanite-, clinopyroxene- and amphibole-bearing calc-alkaline and peralkaline suites and in peraluminous biotite granites, but is preceded by topaz (or cryolite) in strongly peraluminous, Ca-poor granites. The buffered concentrations of fluorine increase in the same order and shift the fluorite occurrence progressively to the late-magmatic stage. These results are in agreement with thermodynamic analysis at 600 °C and 100 MPa (Dolejš and Baker, 2004a), and thus confirm that these equilibria apply over a range of magmatic crystallization temperatures. This thermodynamic analysis is a supplementary tool for interpreting the stability of fluorite vs. topaz or cryolite in relation to multiple liquidus or solidus silicate–oxide assemblages in natural multicomponent systems.

9. Concluding remarks

We have experimentally determined fluorite solubilities in hydrous haplogranitic melts, as a function of the melt aluminosity and independent CaO and F concentrations at 800–950 °C, 100 MPa and H_2O saturation. The results define hyperbolic fluorite saturation isotherms in the CaO–F space, thus suggesting that the fluorite solubility is controlled by activities of CaO and F_2O_{-1} independently. Along the hydrous haplogranite–fluorite binary join, fluorite solubilities exhibit a minimum near subaluminous compositions; the regression of the isotherms for peralkaline, subaluminous and peraluminous experiment sets provides the stoichiometric parameter and the apparent equilibrium constant for fluorite saturation. Both these parameters vary linearly with melt aluminosity, expressed as $Al_2O_3^{exc} = Al_2O_3 - Na_2O - K_2O$ in molar units, and allow calculation of the fluorite isotherm for any whole-rock composition. The thermodynamic interpretation of the experimental results reveals complexing of excess alkalies with fluorine in peralkaline melts and association of excess aluminum with calcium in peraluminous melts, resulting in a minimum in the fluorite solubility at subaluminous composition (cf. Scaillet and Macdonald, 2004).

The fluorite solubility increases with temperature; about twofold in peraluminous and subaluminous melts or threefold in peralkaline melts between 800 and 950 °C. The temperature dependence of the fluorite solubility is described by the binary non-ideal mixing model, i.e., oxygen–fluorine substitution, rather than on the eight-anion basis (Burnham, 1981, 1997). This model fits well the experimental data, does not require temperature dependence of the interaction (Margules) parameter and predicts fluoride–silicate liquid–liquid immiscibility at greater than 1260 °C, in accordance with experimental data on the CaF_2-bearing systems (Mukerji, 1965; Webster et al., 1998).

Comparison of our results with variations of calcium and fluorine concentrations in natural glasses and melt inclusions suggests: (1) Ca vs. F dichotomy in nature corresponds to the shape of fluorite saturation surface (Figs. 1 and 3). An asymptotic approach of saturation isotherms to the concentration axes implies that fluorite crystallization buffers only one of its components (CaO or F), with virtually no dependence on the second. In the Ca-rich magmatic suites, fluorite buffers fluorine concentration in the melt at 0.5 to 0.8 wt.% F (ASI = 0.8 to 1.0), at 800 °C. Considering the temperature increase, this is comparable with 1 wt.% F in the melt at the fluorite–titanite equilibrium at 850 °C, 200 MPa and NNO buffer (Price et al., 1999). On the basis of

thermodynamic calculations, the $\mu(F_2O_{-1})$ decreases, i.e., fluorite stability increases, in the following sequence of mafic-mineral assemblages: enstatite–hornblende, K-feldspar–biotite–hornblende, rutile–titanite, hornblende–diopside and ilmenite–magnetite–titanite.

In the F-rich systems, fluorite solubilities are determined by the calcium concentration and increase with melt peraluminosity. Saturating concentrations vary from ~0.04 to 1.2 wt.% CaO (ASI = 0.88 to 1.2) and suggest suppression of the fluorite crystallization in topaz-bearing Ca-poor granitic and rhyolitic magmas to near-solidus temperatures. In addition, the compatibility of CaO in plagioclase with progressive fractionation of F-bearing granites (e.g., Förster et al., 1999) will result in competing effects of decreasing temperature and decreasing CaO, further reducing the fluorite stability in highly evolved peraluminous melts.

Our experimental results lead to a simple model which allows calculation of the fluorite solubilities and the liquidus isotherms at aqueous-fluid saturation and $p = 100$ MPa for whole-rock composition and temperature of interest. This approach allows evaluation of the conditions of fluorite crystallization in any specific rock composition or the use of magmatic fluorite as a geothermometer.

Acknowledgements

This study represents portion of the senior author's Ph.D. thesis at McGill University, supported by the J. B. Lynch and Carl Reinhardt McGill Major fellowships. Research funding was provided by the Natural Sciences and Engineering Research Council to D.R.B. and by the Geological Society of America and the Society of Economic Geologists student grants to D.D. We appreciate fruitful discussions with Miroslav Štemprok, Robert Linnen, Donald Burt and Rinat Gabitov and thoughtful reviews by Bruno Scaillet and Jonathan D. Price that helped to significantly improve the manuscript. **[RR]**

References

Abdel-Rahman, A.-F.M., El-Kibbi, M.M., 2001. Anorogenic magmatism: chemical evolution of the Mount El-Sibai A-type complex (Egypt), and implications for the origin of within-plate felsic magmas. Geol. Mag. 138, 67–85.

Albarède, F., 1995. Introduction to Geochemical Modeling. Cambridge Univ. Press, Cambridge. 543 pp.

Anderson, G.M., Crerar, D.A., 1993. Thermodynamic in Geochemistry: The Equilibrium Model. Oxford Univ. Press, New York. 588 pp.

Bailey, D.K., Macdonald, R., 1970. Petrochemical variations among peralkaline (comendite) obsidians from the oceans and continents. Contrib. Mineral. Petrol. 28, 340–351.

Barton, M.D., 1982. The thermodynamic properties of topaz solid solutions and some petrologic applications. Am. Mineral. 67, 956–974.

Barton, M.D., 1996. Granitic magmatism and metallogeny of southwestern North America. Spec. Pap.-Geol. Soc. Am. 315, 261–280.

Bevington, P.R., Robinson, D.K., 1992. Data Reduction and Error Analysis for the Physical Sciences. McGraw-Hill, Boston. 328 pp.

Bohlen, S.R., Essene, E.J., 1978. The significance of metamorphic fluorite in Adirondacks. Geochim. Cosmochim. Acta 42, 1669–1678.

Buddington, A.F., Leonard, B.F., 1962. Regional geology of the St. Lawrence County magnetite district, Northwest Adirondacks, New York. U. S. Geol. Surv. Prof. Pap. 376, 1–145.

Burnham, C.W., 1975. Water and magmas; a mixing model. Geochim. Cosmochim. Acta 39, 1077–1084.

Burnham, C.W., 1981. The nature of multicomponent aluminosilicate melts. Phys. Chem. Earth 13–14, 197–229.

Burnham, C.W., 1992. Calculated melt and restite compositions of some Australian granites. Trans. R. Soc. Edinb. Earth Sci. 83, 387–397.

Burnham, C.W., 1994. Development of the Burnham model for prediction of H_2O solubility in magmas. Rev. Miner. 30, 123–129.

Burnham, C.W., 1997. Magmas and hydrothermal fluids. In: Barnes, H.L. (Ed.), Geochemistry of Hydrothermal Ore Deposits. Wiley, New York, pp. 63–123.

Burnham, C.W., Nekvasil, H., 1986. Equilibrium properties of granite pegmatite magmas. Am. Mineral. 71, 239–263.

Burt, D.M., 1972. The influence of fluorine on the facies of Ca–Fe–Si skarns. Year B.-Carnegie Inst. Wash. 71, 443–459.

Candela, P.A., Holland, H.D., 1984. The partitioning of copper molybdenum between silicate melts and aqueous fluids. Geochim. Cosmochim. Acta 48, 373–380.

Chase, M.W. (Ed.), NIST-JANAF Thermochemical Tables, J. Phys. Chem. Ref. Data Monogr., vol. 9. 1951 pp.

Dale, J., Holland, T., Powell, R., 2000. Hornblende–garnet–plagioclase thermobarometry: a natural assemblage calibration of the thermodynamics of hornblende. Contrib. Mineral. Petrol. 140, 353–362.

Dolejš, D., Baker, D.R., 2001. Chemical properties of evolved granitic magmas: the role of fluorine. Abstr.-Geol. Soc. Am. 33, A–333.

Dolejš, D., Baker, D.R., 2003. Stabilities of fluoride minerals in granitic melts: an experimental study and petrological implications. Geol. Assoc. Can. Mineral. Assoc. Can. Abstr. 28, #360.

Dolejš, D., Baker, D.R., 2004a. Thermodynamic analysis of the system Na_2O–K_2O–CaO–Al_2O_3–SiO_2–H_2O–F_2O_{-1}: stability of fluorine-bearing minerals in felsic igneous suites. Contrib. Mineral. Petrol. 146, 762–778.

Dolejš, D., Baker, D.R., 2004b. Thermodynamic model of the Na–Al–Si–O–F melts. Eos Trans.-Am. Geophys. Union 85, #V51C-03 (Suppl.).

Duffy, J.A., 1989. A common optical basicity scale for oxide and fluoride glasses. J. Non-Cryst. Solids 109, 35–39.

Flood, H., Knapp, W.J., 1968. Structural characteristics of liquid mixtures of feldspar and silica. J. Am. Ceram. Soc. 51, 259–263.

Förster, H.-J., Tischendorf, G., Trumbull, R.B., Gottesmann, B., 1999. Late-collisional granites in the Variscan Erzgebirge, Germany. J. Petrol. 40, 1613–1645.

Franck, E.U., Spalthoff, W., 1957. Hydrogen fluoride. I. Specific heat, vapor pressure, and density up to 300° and 300 atmospheres. Z. Elektrochem. 61, 348–357.

Frank, M.R., Candela, P.A., Piccoli, P.M., 1998. K-feldspar–muscovite–andalusite–quartz–brine phase equilibria: an experimental study at 25 to 60 MPa and 400 to 550 °C. Geochim. Cosmochim. Acta 62, 3717–3727.

Frank, M.R., Candela, P.A., Piccoli, P.M., 2003. Alkali exchange equilibria between a silicate melt and coexisting magmatic volatile phase: an experimental study at 800 °C and 100 MPa. Geochim. Cosmochim. Acta 67, 1415–1427.

Frindt, S., Poutiainen, M., 2002. P–T path fluid evolution in the Gross Spitzkoppe granite stock, Namibia. Bull. Geol. Soc. Finl. 74, 103–114.

Fuhrman, M.L., Lindsley, D.H., 1988. Ternary-feldspar modeling and thermometry. Am. Mineral. 73, 201–215.

Gabitov, R., Price, J.D., Gabitov, I.R., Watson, E.B., 2001. Fluorite solubility and diffusivity in haplogranitic melt: preliminary results. Abstr.-Geol. Soc. Am. 33, A-87.

Ghiorso, M.S., Carmichael, I.S.E., Rivers, M.L., Sack, R.O., 1983. The Gibbs free energy of mixing of natural silicate liquids; an expanded regular solution approximation for the calculation of magmatic intensive variables. Contrib. Mineral. Petrol. 84, 107–145.

Ghiorso, M.S., Hirschmann, M.M., Reiners, P.W., Kress III, V.C., 2003. The pMELTS: a revision of MELTS for improved calculation of phase relations and major element partitioning related to partial melting of the mantle to 3 GPa. Geochem. Geophys. Geosyst. 3, 1030. doi:10.1029/2001GC000217.

Guggenheim, E.A., 1967. Thermodynamics. An Advanced Treatment for Chemists and Physicists. Elsevier, New York. 390 pp.

Haapala, I., 1997. Magmatic and postmagmatic processes in tin-mineralized granites: topaz-bearing leucogranite in the Eurajoki rapakivi stock, Finland. J. Petrol. 38, 1645–1659.

Hannon, A.C., Parker, J.M., 2000. The structure of aluminate glasses by neutron diffraction. J. Non-Cryst. Solids 274, 102–109.

Hara, S., Ogino, K., 1981. Density of CaF_2–CaO–Al_2O_3. Can. Metall. Q. 20, 113–116.

Harrison, T.M., Watson, E.B., 1983. Kinetics of zircon dissolution and zirconium diffusion in granitic melts of variable water content. Contrib. Mineral. Petrol. 84, 66–72.

Hildebrand, J.H., 1929. Solubility XII, Regular solutions. J. Am. Chem. Soc. 51, 66–80.

Hildebrand, J.H., Scott, R.L., 1964. The Solubility of Nonelectrolytes. Dover, New York. 488 pp.

Hillert, L., 1964. The phase diagram SiO_2–CaF_2. Acta Chem. Scand. 18, 2411.

Hogan, J.P., Gilbert, M.C., 1995. The A-type Mount Scott granite sheet: importance of crustal magma traps. J. Geophys. Res. 100, 15779–15792.

Holland, T., Powell, R., 1991. A Compensated Redlich-Kwong (CORK) equation for volumes and fugacities of CO_2 and H_2O in the range 1 bar to 50 kbar and 100–1600 °C. Contrib. Mineral. Petrol. 109, 265–273.

Holland, T., Powell, R., 1998. An internally consistent thermodynamic data set for phases of petrological interest. J. Metamorph. Geol. 16, 309–343.

Holland, T., Powell, R., 2001. Calculation of phase relations involving haplogranitic melts using an internally consistent thermodynamic dataset. J. Petrol. 42, 673–683.

Holtz, F., Johannes, W., Pichavant, M., 1992. Effect of excess aluminium on phase relations in the system Qz–Ab–Or: experimental investigation at 2 kbar and reduced H_2O-activity. Eur. J. Mineral. 4, 137–152.

Hudon, P., Jung, I.-H., Baker, D.R., 2003. Melting of β-quartz up to 2.0 GPa and thermodynamic optimization of the silica liquidus up to 6.0 GPa. Phys. Earth Planet. Inter. 130, 159–174.

Jingu, S., Chen, X., Nishimura, S., Oyama, Y., Terashima, K., 2002. Density of molten calcium fluoride. J. Cryst. Growth 237–239, 1797–1801.

Kirschen, M., Pichavant, M., 2001. A thermodynamic model for hydrous silicate melts in the system $NaAlSi_3O_8$–$KAlSi_3O_8$–Si_4O_8–H_2O. Chem. Geol. 174, 103–114.

Kogarko, L.N., Krigman, L.D., 1981. Fluorine in Silicate Melts and Magmas. Nauka, Moscow. 126 pp. (in Russian).

Lentz, D.R., Gregoire, C., 1995. Petrology and mass-balance constraints on major-, trace-, and rare-earth-element mobility in porhyry-greisen alteration associated with the epizonal True Hill granite, southwestern New Brunswick, Canada. J. Geochem. Explor. 52, 303–331.

Lowenstern, J.B., 1994. Chlorine, fluid immiscibility, and degassing in peralkaline magmas from Pantelleria, Italy. Am. Mineral. 79, 353–369.

Lowenstern, J.B., Bacon, C.R., Calk, L.C., Hervig, R.L., Aines, R.D., 1994. Major-element, trace-element, and volatile concentrations in silicate melt inclusions from the tuff of Pine Grove, Wah Wah Mountains, Utah. Open-File Rep.-U. S. Geol. Surv. 94-0242 (20 pp.).

Luth, R.W., 1988. Raman spectroscopic study of the solubility mechanisms of F in glasses in the system CaO–CaF_2–SiO_2. Am. Mineral. 73, 297–305.

Macdonald, R., Smith, R.L., Thomas, J.E., 1992. Chemistry of the subalkalic silicic obsidians. U. S. Geol. Surv. Prof. Pap. 1523 (214 pp.).

Mahood, G.A., Stimac, J.A., 1990. Trace-element partitioning in pantellerites and trachytes. Geochim. Cosmochim. Acta 54, 2257–2276.

Manning, D.A.C., 1981. The effect of fluorine on liquidus phase relationships in the system with Qz–Ab–Or with excess water at 1 kb. Contrib. Mineral. Petrol. 76, 206–215.

Margules, M., 1895. Über die Zusammensetzungen der gesättigten Dämpfe von Mischungen. Sitzungsber. Akad. Wiss. Wien 104, 1243–1278.

Marshall, A.S., Hinton, R.W., Macdonald, R., 1998. Phenocrystic fluorite in peralkaline rhyolites, Olkaria, Kenya Rift Valley. Mineral. Mag. 62, 477–486.

Mediaas, H., Chartrand, P., Tkatcheva, O., Pelton, A.D., Ostvold, T., 2001. Thermodynamic phase diagram calculations and cryoscopic measurements in the NaCl–$CaCl_2$–$MgCl_2$–CaF_2 system. Can. Metall. Q. 40, 33–46.

Mohr, P.J., Taylor, B.N., 2000. CODATA recommended values of the fundamental physical constants: 1998. Rev. Modern Phys. 72, 351–495.

Monier, G., Robert, J.L., 1986. Evolution of the miscibility gap between muscovite and biotite solid solutions with increasing lithium content: an experimental study in the system K_2O–Li_2O–MgO–Al_2O_3–SiO_2–H_2O–HF at 600 °C, 2 kbar PH_2O: comparison with natural lithium micas. Mineral. Mag. 50, 641–651.

Mukerji, J., 1965. Phase equilibrium diagram CaO–CaF_2–$2CaO \cdot SiO_2$. J. Am. Ceram. Soc. 48, 210–213.

Mysen, B.O., Virgo, D., 1985. Interaction between fluorine and silica in quenched melts on the joins SiO_2–AlF_3 and SiO_2–NaF determined by Raman spectroscopy. Phys. Chem. Miner. 12, 77–85.

Mysen, B.O., Cody, G.D., Smith, A., 2004. Solubility mechanisms of fluorine in peralkaline and meta-aluminous silicate glasses and in melts to magmatic temperatures. Geochim. Cosmochim. Acta 68, 2745–2769.

Navrotsky, A., Hon, R., Weill, D.F., Henry, D.J., 1982. Thermochemistry of glasses and liquids in the system $CaMgSi_2O_6$–$CaAl_2SiO_6$–$NaAlSi_3O_8$, SiO_2–$CaAl_2Si_2O_8$–$NaAlSi_3O_8$ and SiO_2–Al_2O_3–CaO–Na_2O. Geochim. Cosmochim. Acta 44, 1409–1433.

Pichavant, M., Valencia Herrera, J., Boulmier, S., Briqueu, L., Joron, J.L., Juteau, M., et al., 1987. The Macusani glasses, SE Peru: evidence of chemical fractionation in peraluminous magmas. In: Mysen, B.O. (Eds.), Magmatic Processes: Physicochemical Principles, Geoch. Soc. Spec. Pub., vol. 1, pp. 359–373.

Pichavant, M., Kontak, D.J., Briqueu, L., Valencia Herrera, J., Clark, A.H., 1988. The Miocene–Pliocene Macusani volcanics, SE Peru. II. Geochemistry and origin of a felsic peraluminous magma. Contrib. Mineral. Petrol. 100, 325–338.

Powell, R., Holland, T., 1993. On the formulation of simple mixing models for complex phases. Am. Mineral. 78, 1174–1180.

Price, J.D., Hogan, J.P., Gilbert, M.C., London, D., Morgan, G.B. VI, 1999. Experimental study of titanite–fluorite equilibria in the A-type Mount Scott granite: implications for assessing F contents of felsic magma. Geology 27, 951–954.

Prigogine, I., Defay, R., 1954. Chemical Thermodynamics. Longmans, Green & Co, London. 543 pp.

Rabinovich, E.M., 1983. On the structural role of fluorine in silicate glasses. Phys. Chem. Glasses 24, 54–56.

Reed, B.C., 1989. Linear least-squares fits with errors in both coordinates. Am. J. Phys. 57, 642–646 (erratum: 58, 189).

Reed, B.C., 1992. Linear least-squares fits with errors in both coordinates. II: comments on parameter variances. Am. J. Phys. 60, 59–62.

Roberts, R.B., White, G.K., 1986. Thermal expansion of fluorites at high temperatures. J. Phys. C. Solid State Phys. 19, 7167–7172.

Ryabchikov, I.D., Solovova, I.P., Babanskii, A.D., Fauzi, K., 1996. Fluorine mobilization and bonding at magmatic and postmagmatic stages in rare-metal granites: evidence from the Homrat Akarem deposit (Egypt). Geochem. Int. 34, 347–350.

Ryerson, F.J., 1985. Oxide solution mechanisms in silicate melts: systematic variations in the activity coefficient of SiO_2. Geochim. Cosmochim. Acta 49, 637–649.

Sakoma, E.M., Martin, R.F., Williams-Jones, A.E., 2000. The late stages of evolution of the Kwandonkaya A-type granite complex, Nigeria, as deduced from mafic minerals. J. Afr. Earth Sci. 30, 329–350.

Sallet, R., Moritz, R., Fontignie, D., 2000. Fluorite $^{87}Sr/^{86}Sr$ and REE constraints on fluid–melt relations, crystallization time span and bulk DSr of evolved high-silica rhyolites, Tabuleiro granites, Santa Catarina, Brazil. Chem. Geol. 164, 81–92.

Scaillet, B., Macdonald, R., 2001. Phase relations of peralkaline silicic magmas and petrogenetic implications. J. Petrol. 42, 825–845.

Scaillet, B., Macdonald, R., 2003. Experimental constraints on the relationships between peralkaline rhyolites of the Kenya rift valley. J. Petrol. 44, 1867–1894.

Scaillet, B., Macdonald, R., 2004. Fluorite stability in silicic magmas. Contrib. Mineral. Petrol. 147, 319–329.

Schaller, T., Dingwell, D.B., Keppler, H., Knoeller, W., Merwin, L., Sebald, A., 1992. Fluorine in silicate glasses: a multinuclear nuclear magnetic resonance study. Geochim. Cosmochim. Acta 56, 701–707.

Schröder, I., 1893. Abhängigkeit der Löslichkeit eines festen Körpers von seiner Schmelztemperatur. Z. Phys. Chem. 9, 449–465.

Seifert, F., Mysen, B.O., Virgo, D., 1982. Three-dimensional network structure of quenched melts (glasses) in the systems SiO_2–$NaAlO_2$, SiO_2–$CaAl_2O_4$, SiO_2–$MgAl_2O_4$. Am. Mineral. 67, 696–717.

Shand, S.J., 1927. Eruptive Rocks: Their Genesis, Composition, and Classification with a Chapter on Meteorites. Wiley, New York. 360 pp.

simmons jr., W.B., Heinrich, E.W., 1975. A summary of the petrogenesis of the granite–pegmatite system in the northern end of the Pikes Peak batholith. Fortschr. Mineral. 52, 251–264.

Spear, F.S., 1993. Metamorphic phase equilibria and pressure–temperature–time paths. Min. Soc. Am. Monogr. 1 (799 pp.).

Stebbins, J.F., Zeng, Q., 2000. Cation ordering at fluoride sites in silicate glasses: a high-resolution 19F NMR study. J. Non-Cryst. Solids 262, 1–5.

Steiner, J.C., Jahns, R.H., Luth, W.C., 1975. Crystallization of alkali feldspar and quartz in the haplogranite system $NaAlSi_3O_8$–$KAlSi_3O_8$–SiO_2–H_2O at 4 kbar. Geol. Soc. Amer. Bull. 86, 83–97.

Taylor, M., Smith, R.W., Ahler, B.A., 1984. Gorceixite in topaz greisen assemblages, Silvermine area, Missouri. Am. Mineral. 69, 984–986.

Thomas, R., Webster, J.D., 2000. Strong tin enrichment in a pegmatite-forming melt. Miner. Depos. 35, 570–582.

Thompson jr., J.B., 1982. Composition space: an algebraic and geometric approach. Rev. Miner. 10, 1–31.

Tindle, A.G., Webb, P.C., 1990. Estimation of lithium contents in trioctahedral micas using microprobe data: application to micas from granitic rocks. Eur. J. Mineral. 2, 595–610.

Tindle, A.G., Breaks, F.W., Selway, J.B., 2002. Tourmaline in petalite-subtype granitic pegmatites: evidence of fractionation and contamination from the Pakeagama Lake and Separation Lake areas of northwestern Ontario, Canada. Can. Mineral. 40, 753–788.

Tischendorf, G., Gottesmann, B., Förster, H.-J., Trumbull, R.B., 1997. On Li-bearing micas: estimating Li from electron microprobe analyses and an improved diagram for graphical presentation. Mineral. Mag. 61, 809–834.

Tischendorf, G., Förster, H.-J., Gottesmann, B., 2001. Tri-und dioktaedrische Glimmer: ein komplexes chemisches System. Z. Geol. Wiss. 29, 275–298.

Tsytsenko, A.K., Frank-Kamenetskaya, O.V., Papuckij, Yu.N., Soltovskaya, I.A., Frank-Kamenetskii, V.A., 1993. Thermal expansion and transition into high-temperature state of crystals CaF_2 and $Ca_{1-x}REE_xF_{2+x}$ (REE-Pr, Nd), $x=0.1$, 0.2. Mineral. Zh. 15, 54–60 (in Russian).

Ueda, S., Maeda, M., 1999. Phase-diagram study for the Al_2O_3–CaF_2–SiO_2 system. Metall. Mater. Trans. 30B, 921–925.

Watson, E.B., 1991. Diffusion in fluid-bearing and slightly-melted rocks: experimental and numerical approaches illustrated by iron transport in dunite. Contrib. Mineral. Petrol. 107, 417–434.

Webster, J.D., Duffield, W.A., 1991. Volatiles and lithophile elements in Taylor Creek rhyolite: constraints from glass inclusion analysis. Am. Mineral. 76, 1628–1645.

Webster, J.D., Duffield, W.A., 1994. Extreme halogen abundances in tin-rich magma of the Taylor Creek rhyolite, New Mexico. Econ. Geol. 89, 840–850.

Webster, J.D., Rebbert, C.R., 2001. The geochemical signature of fluid-saturated magma determined from silicate melt inclusions in Ascension Island granite xenoliths. Geochim. Cosmochim. Acta 65, 123–136.

Webster, J.D., Holloway, J.R., Hervig, R.L., 1987. Phase equilibria of a Be, U and F-enriched vitrophyre from Spor Mountain, Utah. Geochim. Cosmochim. Acta 51, 389–402.

Webster, J.D., Taylor, R.P., Beam, C., 1993. Pre-eruptive composition and constraints on degassing of a water-rich pantellerite magma, Fantale volcano, Ethiopia. Contrib. Mineral. Petrol. 114, 53–62.

Webster, J.D., Burt, D.M., Aguillon, R.A., 1996. Volatile and lithophile trace-element geochemistry of the Mexican tin rhyolite magmas deduced from melt inclusions. Geochim. Cosmochim. Acta 60, 3267–3283.

Webster, J.D., Thomas, R., Rhede, D., Förster, H.-J., Seltmann, R., 1997. Melt inclusions in quartz from an evolved peraluminous pegmatite: geochemical evidence for strong tin enrichment in fluorine-rich and phosphorus-rich residual liquids. Geochim. Cosmochim. Acta 61, 2589–2604.

Webster, J.D., Thomas, R., Veksler, I., Rhede, D., Seltmann, R., Förster, H.-J., 1998. Late-stage processes in P- or F-rich granitic magmas. Acta Univ. Carol., Geol. 42, 181–188.

Weidner, J.R., Martin, R.F., 1987. Phase equilibria of a fluorine-rich leucogranite from the St. Austell pluton, Cornwall. Geochim. Cosmochim. Acta 51, 1591–1597.

Wen, S., Nekvasil, H., 1994. SOLVCALC: an interactive graphics program package for calculating the ternary feldspar solvus and for two-feldspar geothermometry. Comput. Geosci. 20, 1025–1040.

White, R.W., Powell, R., Holland, T.J.B., 2001. Calculation of partial melting equilibria in the system Na_2O–CaO–K_2O–FeO–MgO–Al_2O_3–SiO_2–H_2O (NCKFMASH). J. Metamorph. Geol. 19, 139–153.

Williams, T.J., Candela, P.A., Piccoli, P.M., 1997. Hydrogen–alkali exchange between silicate melts and two-phase aqeuous mixtures: an experimental investigation. Contrib. Mineral. Petrol. 128, 114–126.

Wyllie, P.J., Tuttle, O.F., 1961. Experimental investigation of silicate systems containing two volatile components. Part II. The effects of NH_3 and HF, in addition to H_2O on the melting temperatures of albite and granite. Am. J. Sci. 259, 128–143.

Xiong, X.-L., Rao, B., Chen, F.-R., Zhu, J.-C., Zhao, Z.-H., 2002. Crystallization and melting experiments of a fluorine-rich leucogranite from the Xianghualing Pluton, South China, at 150 MPa and H_2O-saturated conditions. J. Asian Earth Sci. 21, 175–188.

Zeng, Q., Stebbins, J.F., 2000. Fluoride sites in aluminosilicate glasses: high-resolution ^{19}F NMR results. Am. Mineral. 85, 863–867.